JCI The Journal of Clinical Investigation

The gut microbiome controls reactive astrocytosis during Aβ amyloidosis via propionate-mediated regulation of IL-17

Sidhanth Chandra, … , Sangram S. Sisodia, Robert Vassar

J Clin Invest. 2025. https://doi.org/10.1172/JCI180826.

Research In-Press Preview **Immunology** **Microbiology** **Neuroscience**

Accumulating evidence implicates the gut microbiome (GMB) in the pathogenesis and progression of Alzheimer's disease (AD). We recently showed that the GMB regulates reactive astrocytosis and Aβ plaque accumulation in male APPPS1-21 AD model mice. Yet, the mechanism(s) by which GMB perturbation alters reactive astrocytosis in a manner that reduces Aβ deposition remain unknown. Here, we performed metabolomics on plasma from mice treated with antibiotics (abx) and identified a significant increase in plasma propionate, a gut-derived short chain fatty acid, only in male mice. Administration of sodium propionate reduced reactive astrocytosis and Aβ plaques in APPPS1-21 mice, phenocopying the abx-induced phenotype. Astrocyte-specific RNA sequencing on abx and propionate treated mice showed reduced expression of pro-inflammatory and increased expression of neurotrophic genes. Next, we performed flow cytometry experiments where we found abx and propionate decreased peripheral RAR-related orphan receptor-γ (Rorγt)+ CD4+ (Th17) cells and IL-17 secretion, which positively correlated with reactive astrocytosis. Lastly, using an IL-17 monoclonal antibody to deplete IL-17, we found that propionate reduces reactive astrocytosis and Aβ plaques in an IL-17-dependent manner. Together, these results suggest that gut-derived propionate regulates reactive astrocytosis and Aβ amyloidosis by decreasing peripheral Th17 cells and IL-17 release. Thus, propionate treatment or strategies boosting propionate production may represent novel therapeutic strategies for AD.

The gut microbiome controls reactive astrocytosis during Aβ amyloidosis via propionate-mediated regulation of IL-17.

Sidhanth Chandra[1,2], Jelena Popovic[1], Naveen Kumar Singhal[1], Elyse A. Watkins[1], Hemraj B. Dodiya[3], Ian Q. Weigle[3], Miranda A. Salvo[1], Abhirami Ramakrishnan[1], Zhangying Chen[4], James T. Watson[1,5], Aashutosh Shetti[6], Natalie Piehl[1], Xiaoqiong Zhang[3], Leah K. Cuddy[1], Katherine R. Sadleir[1], Steven J Schwulst[4], Murali Prakriya[6], David Gate[1,5], Sangram S. Sisodia[3], Robert Vassar[1,7]

[1]Ken and Ruth Davee Department of Neurology, Northwestern University Feinberg School of Medicine, Chicago, IL 60611, USA

[2]Medical Scientist Training Program, Northwestern University Feinberg School of Medicine, Chicago, IL, 60611, USA.

[3]Department of Neurobiology, University of Chicago, Chicago, IL, 60637 USA

[4]Department of Surgery, Division of Trauma and Critical Care, Northwestern University Feinberg School of Medicine, Chicago, IL, 60611, USA

[5]Abrams Research Center on Neurogenomics, Northwestern University Feinberg School of Medicine, Chicago, IL, 60611, USA.

[6]Department of Pharmacology, Northwestern University Feinberg School of Medicine, Chicago, IL 60611, USA

[7]Mesulam Center for Cognitive Neurology and Alzheimer's Disease, Northwestern University Feinberg School of Medicine, Chicago, IL 60611, USA

Correspondence to:
Robert Vassar
Address: Tarry Building Room 8-71, 300 E Superior, Chicago, Illinois 60611
Phone: 312-503-3361
Email: r-vassar@northwestern.edu

Abstract

Accumulating evidence implicates the gut microbiome (GMB) in the pathogenesis and progression of Alzheimer’s disease (AD). We recently showed that the GMB regulates reactive astrocytosis and Aβ plaque accumulation in male APPPS1-21 AD model mice. Yet, the mechanism(s) by which GMB perturbation alters reactive astrocytosis in a manner that reduces Aβ deposition remain unknown. Here, we performed metabolomics on plasma from mice treated with antibiotics (abx) and identified a significant increase in plasma propionate, a gut-derived short chain fatty acid, only in male mice. Administration of sodium propionate reduced reactive astrocytosis and Aβ plaques in APPPS1-21 mice, phenocopying the abx-induced phenotype. Astrocyte-specific RNA sequencing on abx and propionate treated mice showed reduced expression of pro-inflammatory and increased expression of neurotrophic genes. Next, we performed flow cytometry experiments where we found abx and propionate decreased peripheral RAR-related orphan receptor-γ (Rorγt)+ CD4+ (Th17) cells and IL-17 secretion, which positively correlated with reactive astrocytosis. Lastly, using an IL-17 monoclonal antibody to deplete IL-17, we found that propionate reduces reactive astrocytosis and Aβ plaques in an IL-17-dependent manner. Together, these results suggest that gut-derived propionate regulates reactive astrocytosis and Aβ amyloidosis by decreasing peripheral Th17 cells and IL-17 release. Thus, propionate treatment or strategies boosting propionate production may represent novel therapeutic strategies for AD.

Introduction

Alzheimer's disease (AD) is the most common cause of dementia, a decline in cognition sufficient to impair social and occupational functioning (1). AD is characterized pathologically by the accumulation of proteinaceous aggregates of amyloid beta (Aβ) and tau as well as neuroinflammation in the form of reactive microgliosis and astrogliosis. Additionally, genome-wide association studies implicate innate and adaptive immunity in AD pathogenesis and progression (1). However, the mechanisms governing immunity in AD are still unclear.

Human studies have found that AD patients have an altered gut microbiome (GMB) composition compared to healthy controls, suggesting that these changes in the GMB may play a role in AD pathogenesis and progression (2). AD mouse studies using antibiotic (abx) cocktails to perturb the GMB have consistently shown a reduction in Aβ plaques and neuroinflammatory microglia (3-7). While the connection between the GMB and microgliosis has been well documented, the relationship between the GMB and astrocytes in the context of cerebral amyloidosis has not been extensively investigated (8). We recently reported that abx-mediated GMB perturbation reduces GFAP+ reactive astrocytes, GFAP+ plaque associated astrocytes (PAAs), and astrocytic C3 expression, while inducing homeostatic astrocytic morphology only in male APPPS1-21 mice (9). Notably, fecal matter transplant from untreated APPPS1-21 male mice into abx-treated APPPS1-21 mice to restored the GMB, resulting in a reversal of astrocytic phenotypes, and a restoration of amyloidosis (9). Furthermore, in the context of microglial depletion, abx still reduced GFAP+ reactive astrocytosis, PAAs, and C3 expression (9). However, there were no changes in astrocyte morphology after abx treatment when microglia were depleted. These prior results suggest that abx influences astrocyte phenotypes through both microglial independent and dependent mechanisms (9).

Herein, we studied whether gut-derived metabolites may mediate the connection between the abx-induced GMB compositional changes and brain astrocyte changes. We identified a sex-specific increase in the short-chain fatty acid propionate in male APPPS1-21 mice treated with abx. Similar to abx treatment, administration of sodium propionate to APPPS1-21 mice reduced reactive astrocytosis and Aβ plaques. Through a combination of single-nucleus RNA sequencing (snRNAseq) and astrocyte-specific translating ribosome affinity purification (TRAP) bulk RNA sequencing, we found that abx and propionate reduced astrocytic neuroinflammatory signaling and T-cell recruitment and activation pathways while increasing neurotrophic support pathways. Furthermore, we performed flow cytometry experiments to understand how abx and propionate influenced peripheral immunity. We demonstrate reductions in peripheral RAR-related orphan receptor-γ (Rorγt)+ CD4+ (Th17) cells and IL-17 secretion, which were highly correlated with reactive astrocytosis. Lastly, using an IL-17 monoclonal antibody to deplete IL-17, we found that propionate reduces reactive astrocytosis and Aβ plaques in an IL-17-dependent manner. Collectively, our findings suggest that gut-derived propionate may serve as an endogenous protective metabolite against reactive astrocytosis in AD. Exogenous propionate supplementation or strategies to increase endogenous propionate production may represent novel therapeutic strategies for AD.

Results

Antibiotic-mediated gut microbiome perturbation reduces GFAP+ reactive astrocytes and Aβ plaques while increasing levels of synaptic proteins.

We previously found antibiotic (abx) treatment reduced GFAP+ astrocytes in male APPPS1-21 mice at 9 weeks and 3 months of age, suggesting that the GMB plays a role in regulating reactive astrocytosis in response to amyloidosis (9). In order to perform astrocyte-specific transcriptional studies, we again administered abx or water vehicle (VHL) to APPPS1-21 male mice from postnatal day 14 through 21 (Figure 1A). Similar to our previous report, we found abx treatment reduced microbial diversity and increased cecal/body weight (Supplemental Figure 1A-C). Importantly, abx treatment reduced cortical GFAP+ astrocyte percent area (Figure 1B, C) and there was a trend to reduction of plaque-associated astrocyte (PAA) percent area compared to VHL treated controls at 3 months of age ($p=0.0793$) (Figure 1B, Supplemental Figure 1D). We also found that abx reduced Aβ plaques (Figure 1B, D) and there was a trend toward reduction of Aβ plaque size ($p= 0.0927$) similar to previous reports (Supplemental Figure 1E) (3-6, 9). Although we hypothesize that the abx-mediated reduction in GFAP+ reactive astrocytes is not caused by the decrease in Aβ plaque pathology, we observed a significant positive correlation between GFAP+ reactive astrocytes and Aβ plaques (Figure 1E). This result suggests that higher levels of reactive astrocytes may contribute to Aβ plaque pathology. Similar to our IHC findings, immunoblots of cortical lysates showed a reduction in GFAP levels in abx treated APPPS1-21 mice compared to VHL controls (Supplemental Figure 1F, G). Homeostatic astrocytes are known to have neurotrophic functions and reactive astrocytes are known to contribute to neurodegeneration (10). With this in mind, we asked whether the reduced reactive astrocytosis associated with abx treatment occurred concomitantly with increased presynaptic and postsynaptic levels in these mice. Notably, we found an increase in synaptophysin and PSD-95 levels in these mice (Supplemental Figure 1F, H-I), suggesting abx treatment led to improved synaptic health. Overall, these results suggest that the increased presynaptic and postsynaptic protein levels we observed may be due to a reduction in reactive astrocytosis and potentially increased astrocytic neurotrophic function.

Plasma metabolomics reveals a selective increase in the short chain fatty acid propionate in antibiotic-treated male APPPS1-21 mice that correlates negatively with reactive astrocytosis.

Gut microbial metabolism is often perturbed in diseases involving GMB changes (11). We previously observed abx-induced changes in GMB composition in male APPPS1-21 mice, which were associated with changes in astrocytic phenotypes (9). To determine changes in microbial metabolism that may mediate the effects of GMB changes on astrocytes, we used GC-MS to metabolically profile plasma. Specifically, we analyzed plasma from 9-week-old APPPS1-21 male and female mice that were treated with abx or VHL control (Figure 2A, Supplemental Figure 2). This metabolic assay was designed for increased sensitivity for GMB-derived metabolites. Surprisingly, we found a sex-specific increase in the short chain fatty acid (SCFA) propionate in abx-treated male APPPS1-21 mice but not female mice and did not find significant changes in levels of the SCFAs acetate or butyrate (Figure 2B-D). Additionally, we profiled 13 other metabolites in the plasma and found no changes in abx-treated mice compared to VHL (Supplemental Figure 2). The abx-mediated increase in propionate was particularly interesting because when we previously profiled the GMB composition in these mice, we found only 1 out of the 10 genera which were altered by abx treatment in male mice was increased rather than decreased (9). This genus, *Akkermansia*, was significantly increased by abx treatment only in male APPPS1-21 mice (Supplemental Figure 3A, *Akkermansia* abundance data for these same abx-treated mice were obtained from Chandra et al 2023 (9)), which has been documented in previous studies (4). *Akkermansia* is a SCFA producing bacteria, that produces high levels of propionate (12). Importantly, Spearman correlations of *Akkermansia* levels revealed a positive association with propionate levels. This result suggests that the increase in propionate may be mediated by *Akkermansia* (Supplemental Figure 3B). Propionate levels correlated negatively with measures of reactive astrocytosis, such as GFAP+ astrocytes and complement factor C3 area within GFAP+ astrocytes (Figure 2E, F). Propionate levels correlated positively with homeostatic increases in astrocyte process number and length (trends), which we previously reported increase upon abx treatment in APPPS1-21 male mice (9) (Supplemental Figure 3C, D). Cumulatively, these results suggest that gut-derived propionate may play a role in abx-mediated reduction in reactive astrocytosis and induction of a more homeostatic astrocyte state.

Exogenous sodium propionate administration reduces GFAP+ reactive astrocytosis and amyloidosis.

To test whether propionate mediates abx-induced reductions in GFAP+ reactive astrocytosis, we exogenously administered sodium propionate in drinking water from 1-3 months in male and female APPPS1-21 mice (Figure 3A). Importantly, we found sodium propionate treatment reduced the area occupied by GFAP+ astrocytes (Figure 3B-C) and there was a trend to reduction in PAAs (p= 0.0554) (Figure 3B, Supplemental Figure 4A). Furthermore, sodium propionate treatment reduced Aβ plaques (Figure 3D) and there was a trend to reduction in Aβ plaque size (p=0.1051) (Supplemental Figure 4B). We observed a significant positive correlation between GFAP+ astrocyte percent area and Aβ plaque percent area, suggesting that reactive astrocytes may contribute to Aβ plaque accumulation (Figure 3E). Finally, we profiled levels of SCFAs including propionate in the brain cortex. We found detectable levels in only 1 out of 11 propionate-treated samples (Supplemental Figure 4C). This result suggests that the primary action of propionate occurs in the periphery rather than directly in the brain. Additionally, we found no changes in butyrate or acetate in the cortex of propionate-treated mice compared to vehicle controls (Supplemental Figure 4D-E)

SnRNAseq reveals a reduction in astrocyte neuroinflammatory and development pathways and an increase in neurotrophic subclusters and pathways in APPPS1-21 mice treated with antibiotics.

To determine how astrocyte transcriptional state is altered by abx treatment, we performed single-nucleus RNA sequencing (snRNAseq) on nuclei isolated from cortices of APPPS1-21 male mice that were treated with abx or VHL and sacrificed at 3 months. We sequenced 109,581 nuclei in total. Automated clustering using Seurat yielded 23 total clusters which were manually annotated with classical cell markers (Figure 4A, B, Supplemental Figure 5A). Three of the 23 total clusters were annotated as astrocytes (clusters 3, 22, and 23) by their expression of astrocyte-specific genes (Figure 4A, B, Supplemental Figure 5B).

Interestingly, astrocytes had the most differentially expressed genes (DEGs) when comparing VHL vs abx treatment of any non-neuronal nuclei, (Figure 4C) (DEGs for VHL vs ABX per cluster are in VHL_vs_ABX.zip file). This result suggests that abx-mediated GMB perturbation has a relatively large impact on astrocytic gene expression compared to other cell-types. However, it should be noted that astrocytes were among the most numerous cell type in our analysis, so we had more power to detect DEGs compared to other cell types, such as microglia for which we had much less representation. Cluster 3 contained the most astrocyte nuclei and DEG and pathway analysis via Metascape revealed an increase in neurotrophic pathways such as synapse organization, chemical synaptic transmission, behavior, and memory (Figure 4D, E). Furthermore, we detected a decrease in neuroinflammatory and astrocyte development pathways, such as protein phosphorylation, regulation of MAPK cascade, IL-6 signaling, WNT signaling, and T-cell receptor signaling (Figure 4D, E). Altogether, these results indicate a phenotypic shift of astrocytes in abx-treated APPPS1-21 male mice towards a more homeostatic, neurotrophic state.

To get a better understanding of how abx-induced GMB perturbation alters astrocyte heterogenous subclusters/subtypes, we subclustered all 9758 astrocyte nuclei in their own computational space (Figure 4F). Automated subclustering revealed a total of 6 subclusters (subclusters 0-5) (DEGs for each subcluster are in Table 1). We found changes in the percentages of astrocytes in several of those subclusters in abx treated mice compared to VHL control (Figure 4G). Some subclusters showed reduced astrocyte percentages, such as subclusters 1 (40% reduction) and 3 (28% reduction), which seemed to be enriched in the expression of genes involved in both neurodevelopment and neuroinflammation. Subcluster 1 was enriched in glial cell differentiation, gliogenesis, glial cell development, and astrocyte activation (Supplemental Figure 5). Subcluster 3 was enriched in the expression of genes in pathways such as enzyme-linked receptor protein signaling pathways, gliogenesis, glial cell differentiation, glial cell development, and spinal cord injury (Supplemental Figure 5).

Additionally, some subclusters showed increased percentages of astrocytes in abx compared to VHL, such as subclusters 2 (24% increase), 4 (26% increase), 5 (103% increase), which all appeared to be enriched in homeostatic supportive astrocyte functions (Figure 4H, Supplemental Figure 5). Subcluster 2 was enriched in metabolic and neurotrophic pathways, including synapse organization, neuronal system, and regulation of trans-synaptic signaling (Supplemental Figure 5). Subcluster 4 was enriched in cilium movement, cell projection assembly, and microtubule cytoskeletal organization (Supplemental Figure 5). Subcluster 5 was enriched in pathways such as synapse organization, neuronal system, and regulation of trans-synaptic signaling (Supplemental Figure 5). Together, these data suggest that abx-mediated GMB perturbation reduces astrocytic neuroinflammatory and development subclusters while increasing neurotrophic astrocyte subclusters.

Of note, the mice used for our snRNAseq experiment were housed at the University of Chicago rather than Northwestern University. Because gut microbiota can be influenced by the animal facility location, we profiled the fecal microbiomes of 9-week-old APPPS1-21 mice housed in the two facilities using 16S rRNAseq. We found there were no changes in alpha diversity at a phylum level, but there was reduced alpha diversity at the genus level at Northwestern compared to UChicago (Supplemental Figure 6A, B). Beta-diversity analysis did show a separation of the microbiomes of mice housed at Northwestern compared to UChicago at the phylum and genus levels (Supplemental Figure 6C, D). The difference in the microbial diversity between facilities is a limitation of this experiment. However, it has been previously shown that although GMBs between facilities may be different, similar effects on amyloidosis and neuroinflammation are achieved when using the same combination of abx or other GMB-targeted interventions (3-7, 9, 13).

TRAPseq reveals a decrease in astrocyte neuroinflammatory pathways and an increase and neurotrophic pathways in APPPS1-21 mice treated with antibiotics or propionate.

In addition to snRNAseq, we profiled astrocyte transcriptional/translational state using translating ribosome affinity purification (TRAPseq) bulk RNA sequencing. In TRAPseq, a ribosomal protein L10a is fused to eGFP under the control of a cell type specific promoter in a transgenic mouse model (14). This allows for bead-based immunoprecipitation of polysomal mRNA from specific cell types. Because this method allows for isolation of polysomal mRNA which is being actively translated, the mRNA content profiled should closely resemble the protein content (14). Using the *Aldh1l1-eGFP/Rpl10a* bacTRAP mouse model, we purified polysomal mRNA from astrocytes and performed bulk RNAseq (Figure 5A). We crossed *Aldh1l1-eGFP/Rpl10a* with APPPS1-21 mice, treated the mice with abx, propionate, or VHL and performed TRAPseq (Figure 5A).

Principal component (PC) analysis showed a separation between VHL and abx treated mice with 77% the of variance being explained by the first PC and 8% of the variance being explained by the second PC (Figure 5B). Of note, we observed a potential outlier in the PCA plot, which could be a limitation of the downstream analysis. We found a total of 89 DEGs in abx treated mice compared to VHL in astrocytes (Figure 5C-D) (Table 2). Of the 89 DEGs, 67 were downregulated in abx and 22 were upregulated (Figure 5C-D). Pathway analysis showed that there was in fact a decrease of several pro-inflammatory pathways such as regulation of interferon beta production, positive regulation of T-cell activation, regulation of alpha-beta T-cell activation, regulation of type I interferon production, and positive regulation of T cell-differentiation (Figure 5E). We also observed increases in a few pathways, such as regulation of TP53 activity, ion channel transport, cellular responses to stress and to stimuli (Figure 5E). We validated abx-induced astrocytic gene expression changes by using qPCR to quantify the expression of a subset of genes identified in our TRAPseq experiment: *Gfap*, *Serpina3n*, *Irgm1*, *Bag3*, *Fbxo32*, *Cyp7b1*, *Fezf2* (Supplemental Figure 7). These genes were chosen because they overlapped with those DEGs in our propionate experiment and for which validated commercial primers were available. As expected, our qPCR quantifications of the DEG subset mirrored our TRAPseq results. Altogether, these data indicate that abx primarily reduces astrocytic expression of genes involved in neuroinflammatory response.

We next assessed the effects of propionate treatment on APPPS1-21 mice by TRAPseq. Here, we found a separation of VHL and propionate treated mice in the PC analysis with 37% of variance being explained by the first PC and 16% of the variance being explained by the second PC (Figure 5F). Of note, there are 2 potential outliers observed in the PCA plot in the propionate group, which could be a limitation of the downstream analysis. We identified a total of 1847 DEGs in in astrocytes when comparing propionate treated mice to VHL controls (Figure 5G, H). Of the 1847 DEGs, 862 were downregulated in abx and 984 were upregulated (Figure 5G, H) (Table 3). We found via pathway analysis that propionate treatment increased astrocyte neurotrophic pathways, such as synaptic signaling, cognition, learning or memory, social behavior, and response to metal ion (Figure 5I). Furthermore, propionate decreased expression of genes involved in neurologic disease and inflammatory pathways, including amyotrophic lateral sclerosis, Parkinson disease, fatty acid oxidation, NFκB signaling, T cell factor dependent signaling in response to WNT, class I MHC antigen processing and presentation, and adaptive immune system (Figure 5I).

Since we observed a strong induction of homeostatic astrocyte pathways in abx and propionate treated mouse astrocytes, we next assessed which DEGs upon abx treatment occurred in the context of propionate treatment in our TRAPseq experiments. We found that of 89 DEGs upon abx treatment, 22 of those genes (25%) were significantly regulated in the same direction in propionate treated mice (Supplemental Figure 8A, B). When considering only direction of fold change, comparing abx treatment DEGs with propionate treatment DEGs, 75 (84%) of the genes changed in the same direction (Supplemental Figure 8B). Pathway analysis of the 22 genes that were significantly regulated in the same direction in abx and propionate treated mice primarily revealed a reduction in T-cell activation and differentiation pathways in abx and propionate treated mouse astrocytes compared to controls (Supplemental Figure 8C). These results suggest that abx and propionate may reduce astrocyte mediated T-cell activation and differentiation the setting of Aβ amyloidosis.

Antibiotic and propionate treatment reduce peripheral Th17 cells and IL-17 levels.

It is likely that abx and propionate reduce reactive astrocytosis and amyloidosis mainly through their effect on peripheral immunity since neither reach appreciable concentrations in the brain and brain cells likely do not express the SCFA receptors according to previous studies (15, 16). Therefore, we first performed flow cytometry on cells stained for cell surface markers of various immune cell populations from the spleen, large intestinal (LILN), and small intestinal (SILN) lymph nodes in abx and VHL treated mice (Figure 6A, Supplemental Figure 9, Supplemental Figure 10). We also plated equal amounts of cells from these compartments and re-stimulated the T-cells using CD3/CD28 beads to quantify cytokine release in the media (Figure 6A). Flow cytometry revealed a significant decrease in CD4+ Rorγt+ (Th17) cells in the LILN, a trend to reduction in the SILN, and no change in the spleen in abx treated mice compared to control (Figure 6B). Because we found a reduction in Th17 cells, we quantified levels of their major effector cytokine interleukin-17 (IL-17) released in the media of CD3/CD28 bead restimulated cells (Figure 6C). IL-17 levels were significantly decreased in cells restimulated from the LILN and the SILN but not changed in the spleen in abx mice compared to controls (Figure 6C).

Since we observed that abx likely has its effect on astrocytes through propionate, we also performed flow cytometry on peripheral blood immune cells in propionate treated APPPS1-21 and non-transgenic (NTG) mice and controls (Figure 6D, Supplemental Figure 11). Similar to abx treatment, we found a reduction in Th17 cells in the blood plasma of both APPPS1-21 and NTG mice treated with propionate compared to controls (Figure 6E-G). Because we found in abx treated mice that restimulated T-cells produced lower levels of IL-17 in the LILN, we quantified levels of IL-17 in the large intestinal (LI) lysates and found significantly lower levels of IL-17 in the LI of abx treated APPPS1-21 and NTG mice (trend) compared to controls (Figure 6H-I). Additionally, we observed lower levels of IL-17 in plasma isolated from abx-treated APPPS1-21 (Figure 6J) and NTG (trend) mice compared to controls (Figure 6K). Interestingly, LI IL-17 levels trended toward a positive correlation with LILN TH17 levels ($p= 0.0837$) (Figure 6L), suggesting that IL-17 is likely coming from Th17 cells rather than another source. LI IL-17 levels also correlated positively with plasma IL-17 levels (Figure 6M), indicating that LI-derived IL-17 may also get into the plasma and influence circulating immune or CNS cells. Since we found lower levels of IL-17 in the LI of abx-treated mice, we predicted we would find a similar reduction in propionate-treated mice. Indeed, we found a reduction of LI IL-17 in propionate treated APPPS1-

21 but no change in NTG mice compared to controls (Figure 6N-O). Since we hypothesized that abx- and propionate-mediated reductions in Th17 and IL-17 levels may be the mechanism whereby GFAP+ reactive astrocytosis is reduced in both models, we assessed correlations between LI IL-17 levels and GFAP+ astrocytosis and found significant positive correlations in both treatments (Figure 6P-Q). Additionally, we asked whether there were any changes in immune cell infiltration into the brain parenchyma following propionate treatment. We treated male and female APPPS1-21 mice from 3-6 months with propionate and assessed immune cell populations in the brain using flow cytometry. We chose to treat the mice from 3-6 months because a propionate pilot experiment showed no Th17 cell infiltration at 3 months of age. We found no changes in Th17 cells or other populations following propionate treatment from 3-6 months (Supplemental Figure 12), suggesting that propionate does not influence Th17 cell infiltration into the brain during amyloidosis. We postulate that propionate-induced decreases in peripheral IL-17 traveling to the brain are responsible for reduced cerebral reactive astrocytosis and amyloidosis.

Overall, these results suggest that abx and propionate-mediated reductions in peripheral Th17 cells and IL-17 levels may lead to decreases in GFAP+ reactive astrocytosis and amyloidosis. To determine the relevance of Th17 biology to human AD, we assessed expression of gene markers (17) of Th17 cells in a recent PBMC scRNAseq dataset by Ramakrishnan and colleagues (17, 18). Interestingly, markers of Th17 cells, such as *RORC*, *KLRB1*, *CCR6,* are increased in AD patients compared to healthy controls (Supplemental Figure 13A-C, F). Gaublomme and colleagues previously used scRNAseq to identify GPR65 and FCMR as regulators of Th17 pathogenicity (19). Expression of these markers were also significantly increased in AD patients compared to healthy controls (Supplemental Figure 13D-F). Together these data suggest there may be increased circulating pathogenic Th17 cells in AD that may contribute to disease progression.

Propionate-mediated reduction in GFAP+ reactive astrocytosis and amyloidosis is dependent on IL-17

In order to determine whether the propionate-mediated reductions in reactive astrocytosis and amyloidosis were dependent on IL-17 signaling, we treated male and female APPPS1-21 mice with an IL-17 monoclonal antibody (IL-17 mAb) or IgG1 control to reduce levels of peripheral IL-17. The IL-17 mAb-administered mice were simultaneously treated with saline or sodium propionate (Figure 7A). Compared to mice treated with saline + IgG control, mice treated with saline + IL-17 mAb demonstrated 69% and 40% reductions of IL-17 in plasma and LI, respectively (Figure 7B, C). Similarly, mice treated with propionate + IL-17 mAb had 64% and 47% decreases in IL-17 in the plasma and LI, respectively, compared to saline + IgG control (Figure 7B, C). Interestingly, propionate + IL-17 mAb treatment did not reduce IL-17 levels in the plasma or LI more than saline + IL-17 mAb control, which we speculate is because of the already significant reduction of IL-17 due to IL-17 mAb treatment at the maximum lowering achievable by propionate. Importantly, both the saline + IL-17 mAb and propionate + IL-17 mAb groups had lower Aβ plaque burden, GFAP+ reactive astrocytosis, and PAAs compared to the saline + IgG control group, suggesting that IL-17 reduction alone reduces both GFAP+ reactive astrocytosis and Aβ amyloidosis (trend in the saline + IL-17 mAb group for GFAP; Figure 7D-H). More importantly, there was no change in Aβ amyloidosis, GFAP+ reactive astrocytosis, or PAAs when comparing the saline + IL-17 mAb and propionate + IL-17 mAb groups (Figure 7D-H). This result suggests that propionate-induced reduction in Aβ amyloidosis and GFAP+ reactive astrocytosis is dependent on IL-17 signaling. Furthermore, Pearson’s correlation analysis demonstrated a positive correlation between GFAP+ astrocytosis and Aβ plaque burden suggesting that Aβ plaque burden may be influenced by reactive astrocytosis, at least in part (Figure 7I).

Discussion

GMB composition has been shown to be altered in human AD, indicating that it may play a role in AD pathogenesis and progression (2). Several studies have shown that abx-induced GMB alteration reduces Aβ plaques and microglial activation in AD model mice (3-6, 20). While microglia are important for responding to Aβ pathology in AD, astrocytes also play an important role. We previously showed that abx-mediated GMB perturbation reduces reactive astrocytosis and induces homeostatic morphologic changes through microglial independent and dependent mechanisms respectively in the APPPS1-21 model of amyloidosis (9).

In the current study, we investigated whether abx-mediated changes in reactive astrocytosis and amyloidosis occur through changes in microbial metabolites. Using GC-MS, we found that the SCFA propionate was selectively increased in the plasma of male APPPS1-21 mice after abx treatment compared to controls. Propionate has been found to be reduced in mouse models of AD and human AD patients (21-23). We previously found that bacterial genus *Akkermansia*, which produces propionate at high levels, was also selectively increased in male APPPS1-21 mice compared to controls, suggesting abx-mediated increases in *Akkermansia* may be responsible for elevated levels of plasma propionate (9).

We found that propionate treatment phenocopies abx treatment in that it reduced GFAP+ astrocytosis and amyloidosis. Interestingly, there does not appear to be sex differences following propionate treatment as has been observed after abx treatment. This may be due to the lack of propionate production following abx treatment in females. This could be caused by failure of abx to induce *Akkermansia* or other propionate-producing bacteria and not in the downstream response(s) to propionate.

Using snRNAseq on mouse cortices from APPPS1-21 mice that were treated with abx, we found reductions in neuroinflammatory and neurodevelopmental astrocyte pathways and subclusters and increase in neurotrophic astrocyte pathways and subclusters. Similarly, TRAPseq revealed reductions in neuroinflammatory, and CNS disease associated astrocyte pathways and an increase in neurotrophic astrocyte pathways in abx and propionate treated APPPS1-21 mice compared to controls.

According to previous studies, abx and propionate do not reach high concentrations in the brain parenchyma. Also, we found nearly undetectable levels of propionate in the brains of mice treated with exogenous propionate. Therefore, it is more likely that propionate influences peripheral immunity, which in turn affects reactive astrocytosis (16, 24), rather than a direct effect of propionate on the brain. We found reductions in peripheral Th17 cells and IL-17 levels in APPPS1-21 mice that were treated with abx or propionate. It is well known that Th17 cells are regulated in part by the GMB (25). Propionate has previously been shown to reduce naive T-cell differentiation into Th17 cells in a GPR43 receptor dependent manner (26, 27). Therefore, we contend that abx-mediated increases in propionate reduce differentiation of peripheral Th17 cells and subsequent IL-17 release.

Furthermore, we found that propionate does not directly alter Th17 infiltration into the brain, suggesting that the major direct effect is on peripheral immunity rather than central. It is still an open question as to whether abx treatment or propionate alter Th17 cell infiltration into the brain in later stages of disease which will need to be addressed in future studies.

Interestingly, levels of IL-17 in the LI correlated positively with GFAP+ astrocytosis in both abx and propionate-treated mice. Importantly, using an IL-17 monoclonal antibody, we found that propionate-induced reductions in GFAP+ astrocytosis and Aβ amyloidosis were dependent on IL-

17. These results suggest that propionate controls peripheral IL-17 signaling to regulate reactive astrocytosis and impact amyloidosis.

We believe that abx and propionate induced restoration of an astrocyte homeostatic state occurs through a reduction in peripheral IL-17 signaling. It is possible that this leads to increased ability of astrocytes to directly phagocytose Aβ plaques and instruct microglia to increase their phagocytosis of Aβ plaques. Relatedly, Cao and colleagues found that IL-17 reduced the phagocytic ability of BV-2 microglia (28). It is likely that a similar phenomenon occurs with astrocytes as it is well known that reactive astrocytes have reduced phagocytic ability (10). Furthermore, we previously found complement C3 expression in astrocytes was decreased by abx treatment and C3 derived from astrocytes has been shown to bind to the C3a receptor on microglia and impede microglial phagocytosis of Aβ (9, 29).

There are several limitations of our study. One limitation is that mice were treated with abx from P14-21 which simulates early-life GMB perturbation rather than late-life changes. This was done because the microbiome is more dynamic and amenable to large-scale changes in early-life (5, 6, 30). It will be important for future studies to elucidate the role of late-life GMB perturbation on AD-relevant phenotypes. Herein, we identify propionate as a likely mediator of abx-induced reductions in reactive astrocytosis and amyloidosis. However, it is possible that there may be other gut-derived byproducts or metabolites that mediate the abx phenotype that were not tested in the current study.

Additionally, although we found that abx treatment increases propionate, it should be noted that Seo and colleagues found a decrease in cecal propionate and other SCFAs following abx treatment in Tau PS19 mice with differing APOE genotypes at 40 weeks of age (7). We speculate that the differences between Seo et al. and our study is likely due to combined effects of using amyloid vs tau mouse models, plasma vs cecal sampling, and 9 vs 40-week ages at which SCFAs were measured, and differences in bacteria after abx treatment.

Another limitation of our study is that the snRNAseq was performed on mice housed at the University of Chicago rather than Northwestern University. We have found that the mice housed at the different sites appear to have altered fecal microbiome profiles. However, it has been previously shown that although GMBs between facilities may be different, similar effects on amyloidosis and neuroinflammation are achieved when using the same combination of abx or other GMB-targeted interventions (3-7, 9, 13).

Although our study has found that propionate reduces reactive astrocytosis and amyloidosis, some other studies have found that combinatorial SCFA, including acetate, propionate, and butyrate increases amyloidosis and neuroinflammation in germ-free mice (31). However, it has been shown that acetate by itself increases both amyloidosis and neuroinflammation (24). Comparison of each of the SCFAs administered by themselves on these phenotypes has never been reported to our knowledge. It is likely that SCFAs have different effects and that effects may be dose and timing dependent in amyloid models of AD. We suspect that the SCFA combinatorial studies dilute the protective effects of propionate due to the inclusion of high levels of acetate and excess total SCFA levels. Additionally, germ-free mice have several developmental defects, which makes their study in isolation come with several inherent caveats (15, 32).

Overall, we find that abx-mediated GMB perturbation increases propionate levels in the context of amyloidosis (Figure 8). Both abx and propionate administration reduce levels of peripheral Th17 cells, IL-17, and GFAP+ reactive astrocytosis in the brain (Figure 8). Multi-omic sequencing reveals that both abx and propionate treatment leads to reduction in neuroinflammatory and increases in neurotrophic astrocyte transcriptional programs. These astrocyte changes correspond with reductions in amyloidosis. We postulate a GMB-induced restoration of astrocyte homeostasis restrains Aβ plaques through increased phagocytosis (Figure 8). This reduction in Aβ plaques as well as an increase in neurotrophic support from astrocytes may result in improved neuronal and synaptic health. Our study clarifies molecular mechanisms of GMB and peripheral immunity contributions to reactive astrocytosis and AD. It is possible that the mechanisms elucidated in this study could be harnessed for development of therapeutic strategies for AD. Exogenous sodium propionate treatment given to MS patients over 3 years reduced annual relapse rate, disability stabilization, and brain atrophy compared to controls (33). Our findings suggest that sodium propionate administration may also be efficacious for AD patients. Additionally, increasing endogenous propionate production via *Akkermansia* administration, high fiber diet, or propionate producing engineered probiotics, may prevent the development of amyloidosis and reactive astrocytosis.

Methods

Sex as a biological variable

It has been repeatedly shown that abx treatment only has effects on amyloidosis and neuroinflammation in male but not female amyloid model mice (5, 6, 9). For this reason, we only used male mice for abx treatment, except in our gas chromatography/mass spectrometry (GC-MS) experiment. For our propionate treatment groups, we used both male and female mice because, while abx treatment did not influence amyloidosis or neuroinflammation in females, it was conceivable that propionate treatment may have effects on both sexes.

Animal housing and handling

APPPS1-21 and *Aldh1l1*-eGFP/*Rpl10a* bacTRAP mice were housed in the Northwestern University Center for Comparative Medicine in a specific pathogen free environment. To generate APPPS1-21+/ *Aldh1l1*-eGFP/*Rpl10a*+ mice, hemizygous male APPPS1-21 breeders were crossed to homozygous female *Aldh1l1*-eGFP/*Rpl10a* breeders. For snRNAseq, APPPS1-21 mice were housed in the animal research center at the University of Chicago (only experiment for which mice housed at the University of Chicago were used). All experimental procedures for these mice were approved by the Institutional Animal Care and Use Committee (IACUC) of Northwestern University and the University of Chicago.

Antibiotics treatment

APPPS1-21 male and female mice and wildtype controls were orally gavaged with 200 µL of an antibiotic cocktail (4 mg/ml kanamycin, 0.35 mg/ml gentamicin, 8,500 U/ml colistin, 2.15mg/ml metronidazole, 0.45 mg/ml vancomycin in autoclaved water) or water vehicle from postnatal day (PND)14 to PND 21 as previously described (5, 6, 9). Mice were randomly assigned to antibiotic or water group. Mouse cages were changed each day from PND14 to 21 to avoid consumption of feces from the previous day. Mice were sacrificed and perfused at 9 weeks or 3 months of age, as these ages of APPPS1-21 mice have sufficient neuroinflammation and amyloidosis in the brain cortex, as demonstrated in previous similar studies (5, 6, 9).

Propionate administration

APPPS1-21 male and female mice and wildtype controls were given drinking water containing 150 mM sodium propionate (Sigma #P1880) or 150 mM NaCl (Fisher #S271-1) from 1 month of age to 3 months of age. Doses were selected based on previous studies (24, 34). Mice were randomly assigned to propionate or NaCl group. Mice were perfused and sacrificed at 3 months of age.

IL-17 monoclonal antibody administration

APPPS1-21 male and female mice were randomly assigned and treated with 150 mM saline (Fisher #S271-1) or 150 mM sodium propionate (Sigma #P1880) in their water bottles from 1 month to 3 months of age. In addition, both saline and propionate-treated mice received anti-mouse IL-17A monoclonal antibody (BE0173, Bioxcell) every third day at a dose of 10 mg/kg from 1 month to 3 months of age, similar to previous studies (35-37). A randomly assigned subset of saline-treated control mice were given mouse IgG1 isotype control antibody (BE0083, Bioxcell) following the same dosing schedule. IL-17A levels in plasma and large intestine were measured using a high-sensitivity IL-17 ELISA (MHS170, R&D Systems). Mice were randomly assigned to treatment groups.

Perfusion and tissue preservation

Mice were transcardially perfused at 3 months of age with perfusion buffer containing 20 mg/ml phenylmethylsulfonyl fluoride, 5 mg/ml leupeptin, 200 nM sodium orthovanadate, and 1M dithiothreitol in 1X PBS. Following perfusion, the left hemisphere of the brain was collected for immunohistochemistry and the right hemisphere was sub-dissected into cortex, hippocampus, midbrain, and cerebellum and flash frozen in liquid nitrogen. For TRAPSeq, prior to freezing tissues, all brain regions were washed with a dissection buffer as described by Heiman et al (14) (1× HBSS, 2.5 mM HEPES-KOH, 35 mM glucose, 4 mM NaHCO3, 100 µg/ml cycloheximide in RNase-free water). Dorsal cortex was cut into an approximately 70 mg for TRAPseq and the rest of the ventral cortex was used to make protein lysates. Left brain hemispheres were postfixed in 10% formalin and cryopreserved in 30% sucrose. Left hemispheres were cut into 40 µm sections to be used to for immunohistochemistry. Large intestines were also dissected and cleared with PBS and flash frozen in liquid nitrogen.

Immunohistochemistry

Four comparable sections containing cortex were used for each immunohistochemistry (IHC) experiment. Sections were first washed 3 times in 1X TBS buffer for 5 minutes with agitation. The sections were then incubated in 16 mM glycine with 0.25% triton TBS for an hour at room temperature (RT). After a set of 3x 5-minute washes in TBS, sections were incubated in donkey anti-mouse IgG to minimize background. After 3x 5-minute washes in TBS, sections were incubated overnight in primary antibodies diluted in 1% bovine serum albumin (BSA) in 0.25% triton TBS (1% BSA buffer). The following day, sections were washed 3x for 10 minutes in 1% BSA buffer. The sections were then incubated in secondary antibodies in 1% BSA buffer for 1 hour at RT in the dark. After 3x 5-minute TBS washes, sections were mounted in TBS on Diamond® White Glass Charged Slides (Globe Scientific #1358T). Coverslips (Thermo Fisher #3421) were applied to slides with Prolong Gold reagent (Invitrogen #P36930). Section selection was performed by a person blinded to treatment groups and genotypes.

Microscopy and quantification

Widefield microscopy images were taken in the Northwestern University Center for Advanced Microscopy and Nikon Imaging Center on a Nikon Ti2 widefield microscope with a 10x or 40x air objective. Multiple images were automatically taken and stitched together by the NIS elements software to construct 10X images of each whole brain section. The images were saved as ND2 files and quantified using Nikon NIS elements general analysis tool. Regions of interest of the whole cortex in each section were traced using the NIS region of interest polygon tool. Thresholds for positive signal for each stain were defined in the NIS elements software and then signal was automatically quantified using the batch tool. Image acquisition, image tracing, and quantifications were performed by a person blinded to treatment groups and genotypes.

Antibodies for immunohistochemistry and immunoblotting

For immunohistochemistry the following antibodies were used: chicken anti-GFAP (1:1000, Abcam Ab4674) and mouse anti-Aβ 3D6 (1:1000, Elan Pharmaceuticals). For immunoblotting the following antibodies were used: rabbit anti-GFAP (1:5000, Sigma G9269), mouse anti-SYNAPTOPHYSIN (1:1000, Abcam ab8049), mouse anti-PSD95 (1:2000, Abcam ab192757), rabbit anti-GAPDH (1:5000, Cell Signaling 2118).

GC-MS procedure and data analysis

Short chain fatty acids were derivatized as described by Haak et al (38). with the following modifications. The metabolite extract (100 μL) was added to 100 μL of 100 mM borate buffer (pH 10) (Thermo Fisher, 28341), 400 μL of 100 mM pentafluorobenzyl bromide (Millipore Sigma; 90257) in Acetonitrile (Fisher; A955-4), and 400 μL of n-hexane (Acros Organics; 160780010) in a capped mass spec autosampler vial (Microliter; 09-1200). Samples were heated in a thermomixer C (Eppendorf) to 65 °C for 1 hour while shaking at 1300 rpm. After cooling to RT, samples were centrifuged at 4°C, 2000 x g for 5 min, allowing phase separation. The hexanes phase (100 μL) (top layer) was transferred to an autosampler vial containing a glass insert and the vial was sealed. Another 100 μL of the hexanes phase was diluted with 900 μL of n-hexane in an autosampler vial. Concentrated and dilute samples were analyzed using a GC-MS (Agilent

7890A GC system, Agilent 5975C MS detector) operating in negative chemical ionization mode, using a HP-5MSUI column (30 m x 0.25 mm, 0.25 µm; Agilent Technologies 19091S-433UI), methane as the reagent gas (99.999% pure) and 1 µL split injection (1:10 split ratio). Oven ramp parameters: 1 min hold at 60 °C, 25 °C per min up to 300 °C with a 2.5 min hold at 300 °C. Inlet temperature was 280 °C and transfer line was 310 °C. Data analysis was performed using MassHunter Quantitative Analysis software (version B.10, Agilent Technologies) and confirmed by comparison to authentic standards. Normalized peak areas were calculated by dividing raw peak areas of targeted analytes by averaged raw peak areas of internal standards.

Single nuclei isolation, sequencing, and analysis

Single nuclei suspensions were generated from the cortices of vehicle and antibiotic treated APPPS1-21 male mice housed at the University of Chicago using the 10x Genomics Chromium Nuclei Isolation Kit (#PN-1000494). After isolation, nuclei were loaded into the 10x Genomics Chromium Controller with a target of 10,000 nuclei per sample. Gel bead-in emulsions (GEM) generation and library preparation were performed according to the 10X Chromium Next GEM Single Cell 3' Reagent Kits v3.1 chemistry workflow. Libraries were pooled and sequenced on an Illumina Novaseq 6000 and reads were demultiplexed and aligned to the genome using CellRanger. 109,581 nuclei were sequenced at an average post-normalization read depth of 31,674 reads per cell and 1,736 genes per cell. Data then underwent quality control using SoupX and DoubletFinder R packages. Quality controlled data then was then integrated and multidimensional reduction using uniform manifold approximation and projection (UMAP) plots were produced using Seurat. Differential expression analysis between clusters was performed using Seurat's FindMarkers function. UMAP was manually annotated by using the highly expressed genes in each cluster. Differential expression gene (DEG) analysis between the VHL and abx treated groups was performed using Seurat's FindMarkers function using the masked augmentation subspace training (MAST) algorithm from the R package MAST. The Benjami-

Hochberg (BH) method was used to correct for multiple testing. An FDR corrected p-value of 0.01 with log2FC of 0.25 was the cutoff for significance. Astrocyte clusters were subclustered using the subset function in Seurat. Astrocytes were subclustered using the first 30 principal components at a resolution of 0.1. DEG analysis between astrocyte subclusters was performed using Seurat's FindMarkers function using the MAST algorithm from the R package MAST (Full results can be found in Supplemental Table 1). The Benjami-Hochberg (BH) method was used to correct for multiple testing in astrocyte subcluster DEG analysis. An FDR corrected p-value of 0.001 with log2FC of 0.25 was the cutoff for significance for pathway analysis which was performed using Metascape. Raw sequencing files are available through gene omnibus expression number GSE295459.

Translating ribosome affinity purification (TRAP)

Aldh1l1-eGFP/*Rpl10a* bacTRAP mice incorporate an EGFP-RPL10a ribosomal fusion protein targeted to the astrocyte-specific *Aldh1l1* gene. This animal model enables cell labeling, sorting, and affinity purification of astrocyte-specific polysomal RNAs (14). To capture eGFP+ polysomal complexes in astrocytes for TRAPseq, an anti-GFP affinity matrix (AM) was prepared prior to homogenization of cortical tissue using a previously published protocol (14). Streptavidin MyOne T1 Dynabeads were resuspended, and 450 µL/purification was added to the AM tube. Beads were collected by a magnet and were washed with 1X PBS. 180 µL/purification of biotinylated protein L was then added to the beads and the mixture was incubated on a tube rotator for 35 minutes. The protein L coated beads were captured on a magnet and washed 5 times with 1X PBS containing 3% (w/v) IgG and protease free BSA. 75 µg of anti-GFP antibodies (Htz-GFP-19F7 and Htz-GFP-19C819F7 obtained from Memorial Sloan Kettering Cancer Center Antibody & Bioresource Core Facility) in low salt buffer (20 mM HEPES KOH, 150 mM KCl, 10 mM MgCl2, and 1% (vol/vol) NP-40 in RNase-free water) were then added to the bead mixture and was incubated on a tube rotator for 1 hour. After antibody binding, the final AM was washed 3x with low salt buffer. After washing, the AM was resuspended in a volume of low salt buffer such that each IP received an aliquot of 200 µL. Following AM preparation, flash frozen mouse cortices (washed in dissection buffer before freezing) were homogenized in 1.5 mL tissue lysis buffer (20 mM HEPES KOH, 150 mM KCl, 10 mM MgCl2, EDTA-free protease inhibitor tablet, 0.5 mM DTT, 100 µg/ml cycloheximide in RNase-free water) in a glass tube with an electric homogenizer (Glas-Col #099CK5424) at 900 RPM with 15 full strokes. Lysates were transferred into prechilled microcentrifuge tubes on ice. Post-nuclear supernatants were prepared (S2) by centrifugation at 4°C for 10 minutes at 2000g. S2 was transferred to a new, prechilled microcentrifuge tube on ice. 1/9 sample volume of 10% NP-40 to S2 (final concentration 1%) was added and mixed gently by inverting the tube. 1/9 sample volume of 300 mM DHPC was added to S2 (final concentration 30 mM) and mixed gently by inverting the tube and the mixture was incubated on ice for 5 minutes. Post-mitochondrial supernatants (S20) were prepared by centrifugation at 4°C for 10 minutes at 20,000 xg. S20 was transferred to a new, prechilled microcentrifuge tube. 200 uL of freshly resuspended AM was added to each S20 sample. Beads complexes were washed 4x with high salt buffer (20 mM HERPES, 350 mM KCl, 10 mM MgCl, 1% NP-40 in RNase-free water). RNA was isolated from beads using 100 µL of Nanoprep lysis buffer (from Stratagene Absolutely RNA Nanoprep kit). RNA cleanup was performed according to the kit.

TRAP sequencing and analysis

Quality of RNA isolated from TRAP purifications was assessed using Agilent Bioanalyzer. All RNA used for downstream sequencing had a RIN score above 7. mRNA libraries were generated from TRAP-purified RNA using the Illumina Stranded mRNA prep kit. Prepared libraries were sequenced on an Illumina HighSeq 4000. The quality of reads, in FASTQ format, was evaluated using FastQC. Reads were trimmed to remove Illumina adapters from the 3' ends using cutadapt (Martin, 2011). Trimmed reads were aligned to the Mus musculus genome (mm39) using STAR (Dobin et al, 2013). Read counts for each gene were calculated using htseq-count (Anders et al,

2015) in conjunction with a gene annotation file for mm39 obtained from Ensembl (http://useast.ensembl.org/index.html). Normalization and differential expression were calculated using DESeq2 that employs the Wald test (Love et al, 2014). The cutoff for determining significant DEGs was an FDR-adjusted p-value less than 0.1 using the Benjami-Hochberg method. Pathway analysis was performed using Metascape. (Full results can be found in Supplemental Tables 2-3 for abx and propionate, respectively). Raw sequencing files are available through gene omnibus expression number GSE295458.

Quantitative polymerase chain reaction (qPCR)

RNA isolated via TRAP protocol as described above was converted to cDNA using Invitrogen Superscript IV VILO Mastermix Kit (cat #11766050). The mastermixes for qPCR were made by using TaqMan fast advanced master mix (cat #4444556) and TaqMan single tube gene expression assay primers against Gfap (ThermoFisher Mm01253033_m1), Serpina3n (ThermoFisher Mm00776439_m1), Irgm1 (ThermoFisher Mm00492596_m1), Bag3 (ThermoFisher Mm00443474_m1), Fbxo32 (Mm00499523_m1), Cyp7b1 (ThermoFisher Mm00484157_m1, Fezf2 (ThermoFisher Mm01320619_m1). Experimental primers were normalized to *Gapdh* (ThermoFisher Hs02786624). Reactions were run on a 96 well plate in an Applied Biosystems QuantStudio 7 flex machine (cat #448701) in the Northwestern NUSeq core facility. The protocol used for amplification contained a 2-min hold step at 50 °C, a 2-min hold step at 95 °C, and 40 cycles of 1 s at 95 °C followed by 20 s at 60 °C. Genes selected for this qPCR validation analysis were DEGs shared between abx and propionate analysis for which validated primers were available through ThermoFisher (≥2 citations).

Flow cytometry

Mesenteric (large intestinal and small intestine-draining) lymph nodes (LN), spleen, or plasma were isolated from mice. LNs were digested for 45 min at 37°C in DMEM with collagenase IV (1 mg/ml; Worthington). LN and spleen were homogenized using syringe plungers onto 70 mM strainers. Spleens were lysed using 3-ml ACK lysis buffer (Gibco) for 5 min and quenched with 30 ml of DMEM. Cells were counted using a cell counter (Contessa). Single-cell suspensions of LNs, spleen, or plasma were plated in U-bottom 96-well plates. Cells were washed in PBS and stained for 15 min at 4°C with Live/Dead Fixable Dye and 1:200 Fc Block. Cells were washed in PBS + 2% fetal bovine serum (FBS) and stained for 30 min at 4°C with surface antibodies at a 1:200 dilution. For intracellular cytokine staining, cells were fixed in 2% paraformaldehyde and permeabilized in 0.1% saponin. Cells were washed twice in permeabilization buffer and stained in permeabilization buffer for 30 min at 4°C. Cells were washed twice in permeabilization buffer and resuspended in PBS + 2% FBS for analysis. For transcription factor staining, cells were fixed and permeabilized for 50 min at 4°C (FoxP3/Transcription Factor Kit, eBioscience). Cells were washed twice and stained for 1 hour in permeabilization buffer. Cells were washed twice and resuspended in PBS + 2% FBS. Data were acquired on an LSRFortessa or BD FACSymphony (BD Bioscience) and analyzed by FlowJo. For information on markers of cell populations see Supplemental Table 4.

Ex vivo restimulation

For 3-day ex vivo restimulation, 320,000 splenocytes or 120,000 LN cells were plated in a 96-well round bottom plate and cells were stimulated with 2 mL CD3/CD28 beads. After 3 days, the supernatant was taken for cytokine analysis via enzyme-linked immunosorbent assay (ELISA).

Protein lysate generation and ELISAs

Large intestine and brain lysates were generated by homogenizing large intestinal tissue (washed with PBS during initial dissection) using a handheld electronic homogenizer in 1 mL of RIPA buffer (50mM tris, 0.15 M NaCl, 1% octylphenoxypolyethoxyethanol (IGEPAL), 0.1% SDS, and 0.5% sodium deoxylate at pH8) containing protease (cat # 535140, Calbiochem) and phosphatase inhibitor (cat # 78427 Thermo Fisher Scientific) cocktails. Samples were incubated for 30 mins on ice and then sonicated for 20 seconds each. The samples were then centrifuged at 14,000 xg for 30 mins and supernatant was collected (RIPA soluble fraction). Protein concentration was determined using Pierce BCA Protein Assay kit. IL-17 ELISAs were performed using both regular (cat # BMS6001, Thermo Fisher Scientific) and high sensitivity kits (cat # MHS170, R & D Systems).

Mouse brain flow cytometry

APPPS1-21 mice were treated with 150 mM sodium propionate (Sigma #P1880) or 150 mM NaCl (Fisher #S271-1) from 3 month of age to 6 months of age. Mouse brains were harvested and the left hemibrain was dissected for brain cell isolations. Specifically, the left hemisphere was injected with 3 mL of digestion buffer made of 2.5 mg/mL Liberase TL and 1 mg/mL DNase I in HBSS (Roche, Basel, Switzerland), morcellated, and rapidly transferred to C-tubes. Tissue in C-tubes was then dissociated using a MACS dissociator according to the manufacturer’s instructions. The dissociated tissue was strained through a 40-µm nylon mesh strainer and washed with 100 mL of autoMACs running buffer per brain. C-tubes, MACS dissociator, and autoMACs running buffer are all from Miltenyi Biotec (North Rhine-Westphalia, Germany). Cell debris was removed using the Debris Removal Solution (130-109-398; Miltenyi Biotec) and brain-derived single cell suspension was made according to the manufacturer’s guideline.

Cell surface staining was performed using the following antibodies: Fixable Viability Dye eFluor 506 (65-0866-14; Invitrogen), CD45 BUV661 (1:400, 612975, clone: 30-F11; BD Biosciences), CD11b-APC-Cy7 (1:1000, A15390, clone: M1/70; Invitrogen), Ly6C BV421 (1:1000, 562727, clone: AL-21; BD Biosciences), TCRgd BUV737 (1:200, 748991, clone: GL3; BD Bioscences), CD3e BUV396 (1:100, 563565, clone: 145-2C11; BD Biosciences), CD8 PerCP-Cy5.5(1:67, 1299159, clone: 53-6.7; BD Biosciences), CD4 AF700(1:333, 557956, clone: RM4-5; BD

Biosciences), CD64 BV786 (1:83, 741024, clone: X54-5/7.1; BD Biosciences), MHCII BV605 (1:200, 563413, clone: M5/114.15.2; BD Biosciences), CD25 PE-Cy7 (1:200, 552880, clone: PC61; BD Biosciences). For intracellular staining, Foxp3/Transcription Factor Staining Buffer Set (00-5523099; eBioscience) was used following the provider guidelines. The following antibodies for intracellular staining were used: Tbet BV711 (1:40, 644819, clone: 4B10; BioLegend), GATA3 PE (1:100, 12-9966-42, clone: TWAJ; Invitrogen), and RORγt Alexa Fluor 647 (1:400, 562682, clone: Q31-378; BD Biosciences). Stained cells were then analyzed on a BD FACSymphony flow cytometer (BD Biosciences), and analysis was performed using flowJo software (version 10.0). CD4+ CD25+ FOXP3+ T-regulatory cells, TCRgd+ T cells, and CD4+ GATA3+ Th2 cells were not detected.

Immunoblotting

Protein lysates were diluted to 2 μg/μl and for immunoblots 18 μg of total protein was mixed with 4 × Laemmli buffer (cat # 1610747, Bio-Rad) and heated at 95 °C for 10 min. The samples were then run on 4–12% Criterion XT Bis–Tris polyacrylamide gels (cat # 3450126, Bio-Rad) in MES buffer. Gels were transferred to 0.45 μm nitrocellulose membranes (cat # 1620167, Bio-Rad) using the Bio-Rad Trans-blot Turbo Transfer System. Membranes were briefly incubated in 0.1% ponceau solution to assess transfer quality. After 3 × 5 min washes in TBST, membranes were incubated in 5% milk in TBST for 1 h. Primary antibodies were incubated in 5% milk overnight at 4 °C, and secondary antibodies were incubated in 5% milk for 1 h at room temperature (antibodies listed in Additional file 10). After two TBST and one TBS 5 min washes, membranes were incubated in SuperSignal West Pico Plus Chemilumeniscent substrate (cat # 34580, Thermo Scientific). Membranes were imaged on a Bio-Rad imager and analyzed using ImageLab software. Uncropped blots are available in Supplemental Figure 14.

Basic processing of 16S amplicon sequencing data

Forward and reverse reads were merged using PEAR v0.9.11. Merged reads were trimmed with cutadapt v4.4 to remove ambiguous nucleotides, primer sequences, and trimmed based on quality threshold of p = 0.01 (Martin, 2011). Reads that were less than 225 bp after trimming were discarded. Chimeric sequences were identified and removed with VSEARCH v2.25.0 using the UCHIME algorithm with a comparison to Silva v138.1 reference sequence. Amplicon sequence variants (ASVs) were identified using DADA2 v1.30.0. The representative sequences for each ASVs were then annotated, taxonomically using the Naïve Bayesian classifier included in DADA2 with the Silva v138.1 training set.

Differential analysis of Akkermansia (data from Chandra et al., 2023 (9))

Differential analyses of taxa as compared with site were performed using the software package edgeR on raw sequence counts . Prior to analysis the data were filtered to remove any sequences that were annotated as chloroplast or mitochondria in origin as well as removing taxa that accounted for less than 100 total counts and were present in less than 30% of the sample. Data were normalized as counts per million. Normalized data were then fit using a negative binomial generalized linear model using experimental covariates, and statistical tests were performed using a likelihood ratio test. Adjusted p values (q values) were calculated using the Benjamini-Hochberg false discovery rate (FDR) correction. Significant taxa were determined based on an FDR threshold of 5% (0.05). The data from this differential analysis is from Chandra et al 2023 (9).

Alpha Diversity analyses

Shannon indices and richness (i.e. species number) were calculated with default parameters in R using the vegan library (Oksanen et al., 2018). Prior to analysis, the data were rarefied to a depth of 10,000 counts per sample. The resulting Shannon indices were then modelled with the sample covariates using a generalized linear model (GLM) assuming a Gaussian distribution.

Significance of the model (ANOVA) was tested using the F test. Post-hoc tests were performed using Kruskal-Wallis test. Plots were generated in R using the ggplot2 library (Wickham, 2009).

Beta Diversity/Dissimilarity analyses

Bray-Curtis indices were calculated with default parameters in R using the vegan library (Oksanen et al., 2018). Prior to analysis the normalized data were square root transformed. The resulting dissimilarity indices were modelled and tested for significance with the sample covariates using the ANOSIM test. Plots were generated in R using the ggplot2 library (Wickham, 2009).

Statistics

Statistical analysis was performed using GraphPad Prism 9 software for all studies (Figures 1-3, 6-7 and Supplemental Figures 1-4, 7, and 10-12) except the RNA sequencing studies. With the exception of the RNA sequencing studies, comparisons between two groups were performed using two-tailed unpaired student's t-tests (Figures 1-3, 6, and Supplemental Figures 1-4, 7, and 10-12). Multiple comparisons were performed using one or two-way analysis of variance (ANOVA) (Figures 2, 7, Supplemental Figure 3). Pearson's correlation coefficients and two-tailed p-values were calculated using GraphPad Prism 9 with a confidence interval of 95%. Spearman's correlation coefficients and two-tailed p-values were calculated for Figure 2I.

Study approval

All experimental procedures for these mice were approved by the IACUC of Northwestern University and the University of Chicago.

Data availability

All data represented in the study are available in supporting data file 1. Sequencing and GC-MS raw files can be shared upon request.

Author contributions

S. Chandra and R. Vassar conceived the study. Schwulst SJ, M Prakriya, D Gate, and SS Sisodia provided guidance as the study evolved. S. Chandra, J. Popovic, NK Singhal, EA Watkins, HB Dodiya, I. Q. Weigle, M. Salvo, A. Ramakrishnan, Z. Chen, A Shetti, X. Zhang, L. Cuddy, and K. Sadlier, performed the experiments. J Watson and N. Piehl helped perform bioinformatic analysis on snRNAseq data. S. Chandra and R. Vassar wrote the manuscript. D. Gate and SS Sisodia helped edit the manuscript. All authors read and approved the final manuscript.

Conflicts of Interest

The authors have declared that no conflict of interest exists.

Acknowledgements

Imaging work for this study was performed at the Northwestern University Center for Advanced Microscopy generously supported by NCI CCSG P30 CA060553 awarded to the Robert H Lurie Comprehensive Cancer Center. We would especially like to thank David Kirchenbuechler for his assistance with imaging and analysis. We would like to acknowledge the Host-Microbe Metabolomics Facility (HMMF) in the Duchossois Family Institute at the University of Chicago for performing the metabolomics studies. We would also like to thank the University of Illinois Chicago Genome Research Core and the Research Informatics Core for their assistance with the microbiome profiling studies and basic processing of the raw data associated with these studies. George E. Chlipala from UIC helped preform the analysis and is supported in part by NCATS through Grant UL1TR002003. RNA sequencing studies were performed using the Northwestern NUseq core facility. Our sources of funding for this project were from Open Philanthropy/Good Ventures Foundation (to R. Vassar, S. Sisodia), Cure Alzheimer's Fund (to R. Vassar, S. Sisodia), and the Luminescence Foundation (to S. Sisodia). This funding was the primary funding mechanism for the study. S. Chandra was supported by F30AG079577 (to S. Chandra) and

NIGMS T32GM008152 (to Northwestern University Medical Scientist Training Program). Additional funding sources included NINDS R00 NS112458 and NIA R01 AG078713 (to D. Gate). E. Watkins was supported by NHLBI 5T32HL007909 and M. Salvo was supported by NIA 5T32AG020506 (to R. Vassar).

References

1. Long JM, and Holtzman DM. Alzheimer Disease: An Update on Pathobiology and Treatment Strategies. *Cell.* 2019;179(2):312-39.
2. Vogt NM, et al. Gut microbiome alterations in Alzheimer's disease. *Scientific Reports.* 2017;7(1):13537.
3. Minter MR, et al. Antibiotic-induced perturbations in gut microbial diversity influences neuro-inflammation and amyloidosis in a murine model of Alzheimer's disease. *Scientific reports.* 2016;6:30028-.
4. Minter MR, et al. Antibiotic-induced perturbations in microbial diversity during post-natal development alters amyloid pathology in an aged APP(SWE)/PS1(ΔE9) murine model of Alzheimer's disease. *Sci Rep.* 2017;7(1):10411.
5. Dodiya HB, et al. Sex-specific effects of microbiome perturbations on cerebral Aβ amyloidosis and microglia phenotypes. *J Exp Med.* 2019;216(7):1542-60.
6. Dodiya HB, et al. Gut microbiota–driven brain Aβ amyloidosis in mice requires microglia. *Journal of Experimental Medicine.* 2021;219(1):e20200895.
7. Seo DO, et al. ApoE isoform- and microbiota-dependent progression of neurodegeneration in a mouse model of tauopathy. *Science.* 2023;379(6628):eadd1236.
8. Chandra S, and Vassar R. The role of the gut microbiome in the regulation of astrocytes in Alzheimer's disease. *Neurotherapeutics.* 2024;21(6):e00425.
9. Chandra S, et al. The gut microbiome regulates astrocyte reaction to Aβ amyloidosis through microglial dependent and independent mechanisms. *Molecular Neurodegeneration.* 2023;18(1):45.
10. Liddelow SA, et al. Neurotoxic reactive astrocytes are induced by activated microglia. *Nature.* 2017;541(7638):481-7.
11. Chandra S, and Vassar RJ. Gut microbiome-derived metabolites in Alzheimer's disease: Regulation of immunity and potential for therapeutics. *Immunol Rev.* 2024;327(1):33-42.

12. Cani PD, et al. Akkermansia muciniphila: paradigm for next-generation beneficial microorganisms. *Nature Reviews Gastroenterology & Hepatology.* 2022;19(10):625-37.

13. Bosch ME, et al. Sodium oligomannate alters gut microbiota, reduces cerebral amyloidosis and reactive microglia in a sex-specific manner. *Molecular Neurodegeneration.* 2024;19(1):18.

14. Heiman M, et al. Cell type–specific mRNA purification by translating ribosome affinity purification (TRAP). *Nature Protocols.* 2014;9(6):1282-91.

15. Erny D, et al. Host microbiota constantly control maturation and function of microglia in the CNS. *Nature Neuroscience.* 2015;18(7):965-77.

16. Dodiya HB, et al. Synergistic depletion of gut microbial consortia, but not individual antibiotics, reduces amyloidosis in APPPS1-21 Alzheimer’s transgenic mice. *Scientific Reports.* 2020;10(1):8183.

17. Annunziato F, et al. Defining the human T helper 17 cell phenotype. *Trends Immunol.* 2012;33(10):505-12.

18. Ramakrishnan A, et al. Epigenetic dysregulation in Alzheimer's disease peripheral immunity. *Neuron.* 2024.

19. Gaublomme JT, et al. Single-Cell Genomics Unveils Critical Regulators of Th17 Cell Pathogenicity. *Cell.* 2015;163(6):1400-12.

20. Mezö C, et al. Different effects of constitutive and induced microbiota modulation on microglia in a mouse model of Alzheimer's disease. *Acta Neuropathol Commun.* 2020;8(1):119.

21. Xie J, et al. Gut microbiota regulates blood-cerebrospinal fluid barrier function and Aβ pathology. *The EMBO Journal.* 2023;42(17):e111515.

22. Wu L, et al. *Nutrients*. 2021.

23. Zheng J, et al. Stable isotope labeling combined with liquid chromatography-tandem mass spectrometry for comprehensive analysis of short-chain fatty acids. *Analytica Chimica Acta.* 2019;1070:51-9.

24. Erny D, et al. Microbiota-derived acetate enables the metabolic fitness of the brain innate immune system during health and disease. *Cell Metab.* 2021;33(11):2260-76.e7.

25. Sun C-Y, et al. T helper 17 (Th17) cell responses to the gut microbiota in human diseases. *Biomedicine & Pharmacotherapy.* 2023;161:114483.

26. Du HX, et al. Gut Microflora Modulates Th17/Treg Cell Differentiation in Experimental Autoimmune Prostatitis via the Short-Chain Fatty Acid Propionate. *Front Immunol.* 2022;13:915218.

27. Haghikia A, et al. Dietary Fatty Acids Directly Impact Central Nervous System Autoimmunity via the Small Intestine. *Immunity.* 2015;43(4):817-29.

28. Cao M, et al. IL-17A promotes the progression of Alzheimer’s disease in APP/PS1 mice. *Immunity & Ageing.* 2023;20(1):74.

29. Lian H, et al. Astrocyte-Microglia Cross Talk through Complement Activation Modulates Amyloid Pathology in Mouse Models of Alzheimer's Disease. *J Neurosci.* 2016;36(2):577-89.

30. Chandra S, et al. The gut microbiome in Alzheimer’s disease: what we know and what remains to be explored. *Molecular Neurodegeneration.* 2023;18(1):9.

31. Colombo AV, et al. Microbiota-derived short chain fatty acids modulate microglia and promote Aβ plaque deposition. *eLife.* 2021;10:e59826.

32. Luczynski P, et al. Growing up in a Bubble: Using Germ-Free Animals to Assess the Influence of the Gut Microbiota on Brain and Behavior. *International Journal of Neuropsychopharmacology.* 2016;19(8):pyw020.

33. Duscha A, et al. Propionic Acid Shapes the Multiple Sclerosis Disease Course by an Immunomodulatory Mechanism. *Cell.* 2020;180(6):1067-80.e16.

34. Smith PM, et al. The microbial metabolites, short-chain fatty acids, regulate colonic Treg cell homeostasis. *Science.* 2013;341(6145):569-73.

35. Naik S, et al. Commensal-dendritic-cell interaction specifies a unique protective skin immune signature. *Nature.* 2015;520(7545):104-8.

36. Hofstetter HH, et al. Therapeutic efficacy of IL-17 neutralization in murine experimental autoimmune encephalomyelitis. *Cell Immunol.* 2005;237(2):123-30.

37. Burrell BE, et al. CD8+ Th17 mediate costimulation blockade-resistant allograft rejection in T-bet-deficient mice. *J Immunol.* 2008;181(6):3906-14.

38. Haak BW, et al. Impact of gut colonization with butyrate-producing microbiota on respiratory viral infection following allo-HCT. *Blood.* 2018;131(26):2978-86.

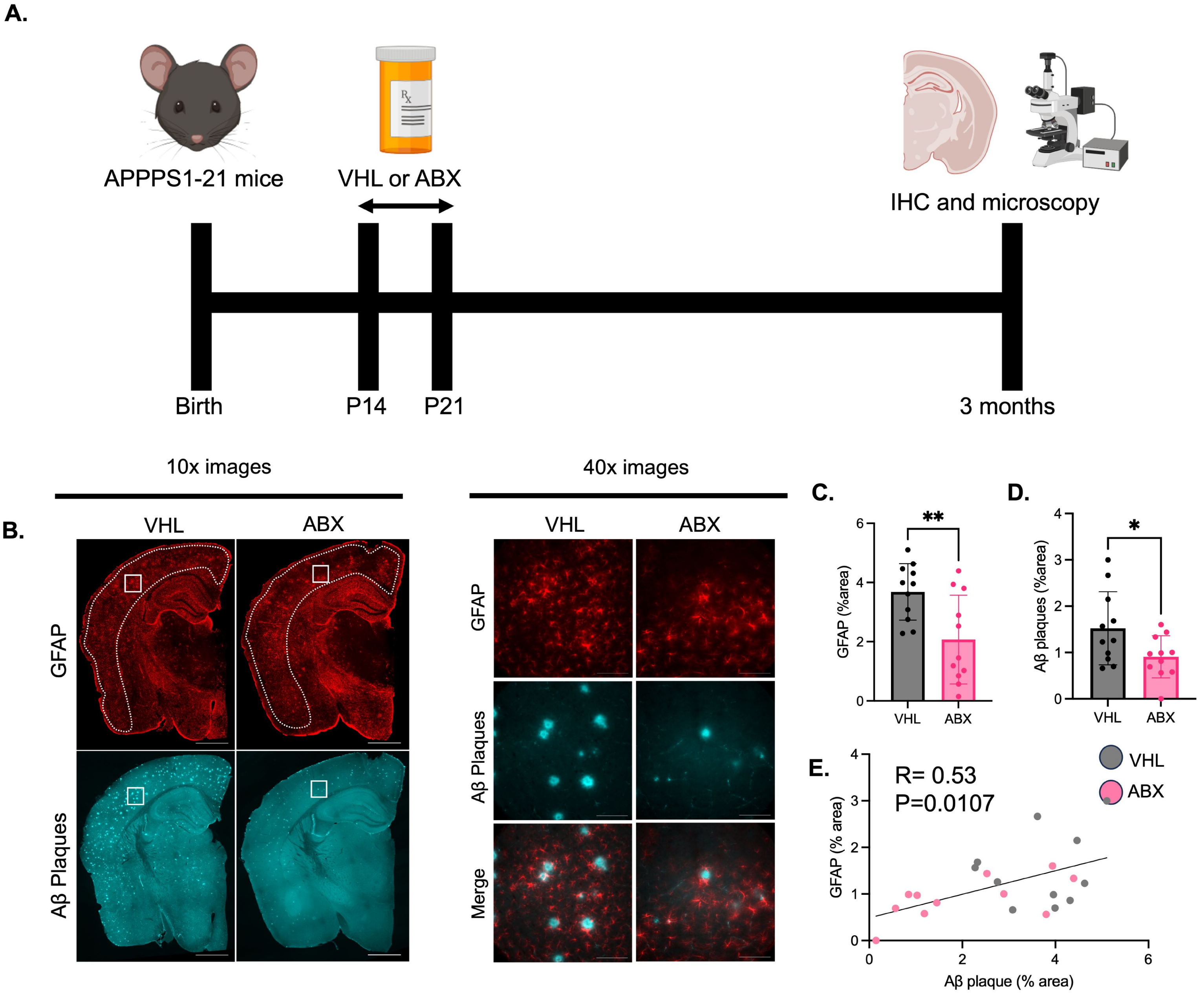

Figure 1: Antibiotic-mediated gut microbiome perturbation reduces GFAP+ astrocytes and Aβ plaques in the cortex of APPPS1-21 male mice.

(A) Schematic depicting experimental paradigm. (B) Representative images of whole brain sections (10x) and high magnification images of cortex (40x) stained for GFAP+ positive astrocytes and Aβ plaques in APPPS1-21 male mice treated with antibiotics (ABX) or vehicle (VHL) control. Quantification of cortical (C) GFAP+ astrocyte percent area and (D) Aβ plaque percent area in VHL and ABX treated APPPS1-21 mice. (E) Pearson's correlation analysis between GFAP+ astrocyte percent area and Aβ plaque percent area in VHL and ABX treated APPPS1-21 mice. Data expressed as mean ± standard deviation. N = 11/group. Statistics calculated using two-tailed unpaired student's t-tests. 4 sections used per animal. * denotes a p-value ≤ 0.05, ** indicates p-value ≤ 0.01. Scale bar indicates 1000 µm in 10x images and 100 µm in 40x images. Dotted lines indicate analyzed area of cortex.

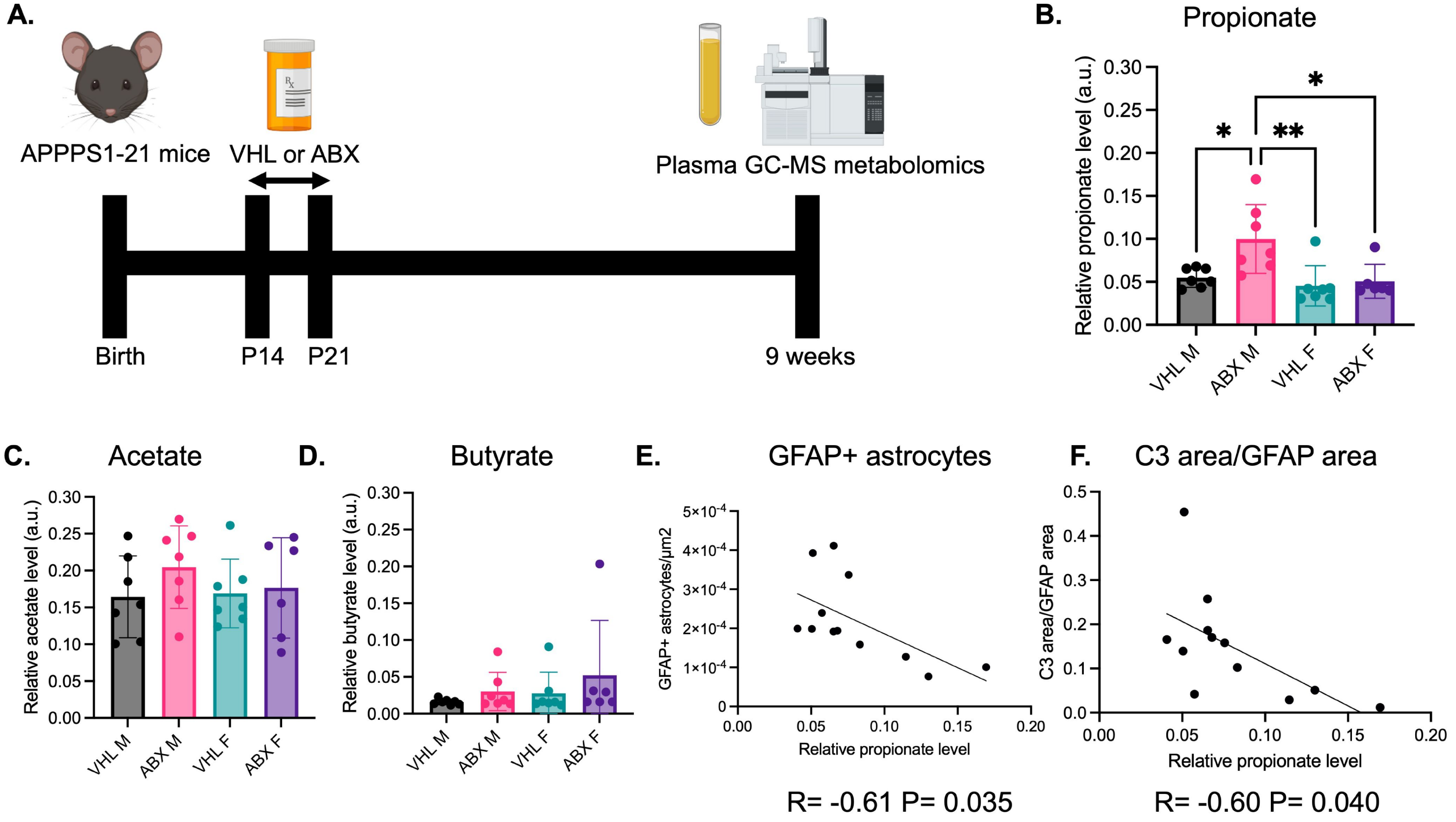

Figure 2: Antibiotic-mediated gut microbiome perturbation increases plasma propionate levels which negatively correlate with reactive astrocytosis in APPPS1-21 male mice.

(A) Schematic depicting experimental paradigm. Relative GC-MS quantification of the short chain fatty acids (B) propionate, (C) acetate, and (D) butyrate in the plasma of vehicle (VHL) and antibiotic (ABX) treated APPPS1-21 male (M) and female (F) mice. Pearson's correlation analysis between (E) GFAP+ astrocyte percent area and (F) C3 area/GFAP area and plasma propionate levels in VHL and ABX treated male APPPS1-21 mice. Data expressed as mean ± standard deviation. N = 6-7/group. Statistics calculated using two-way ANOVA. * denotes a p-value ≤ 0.05, ** indicates p-value ≤ 0.01.

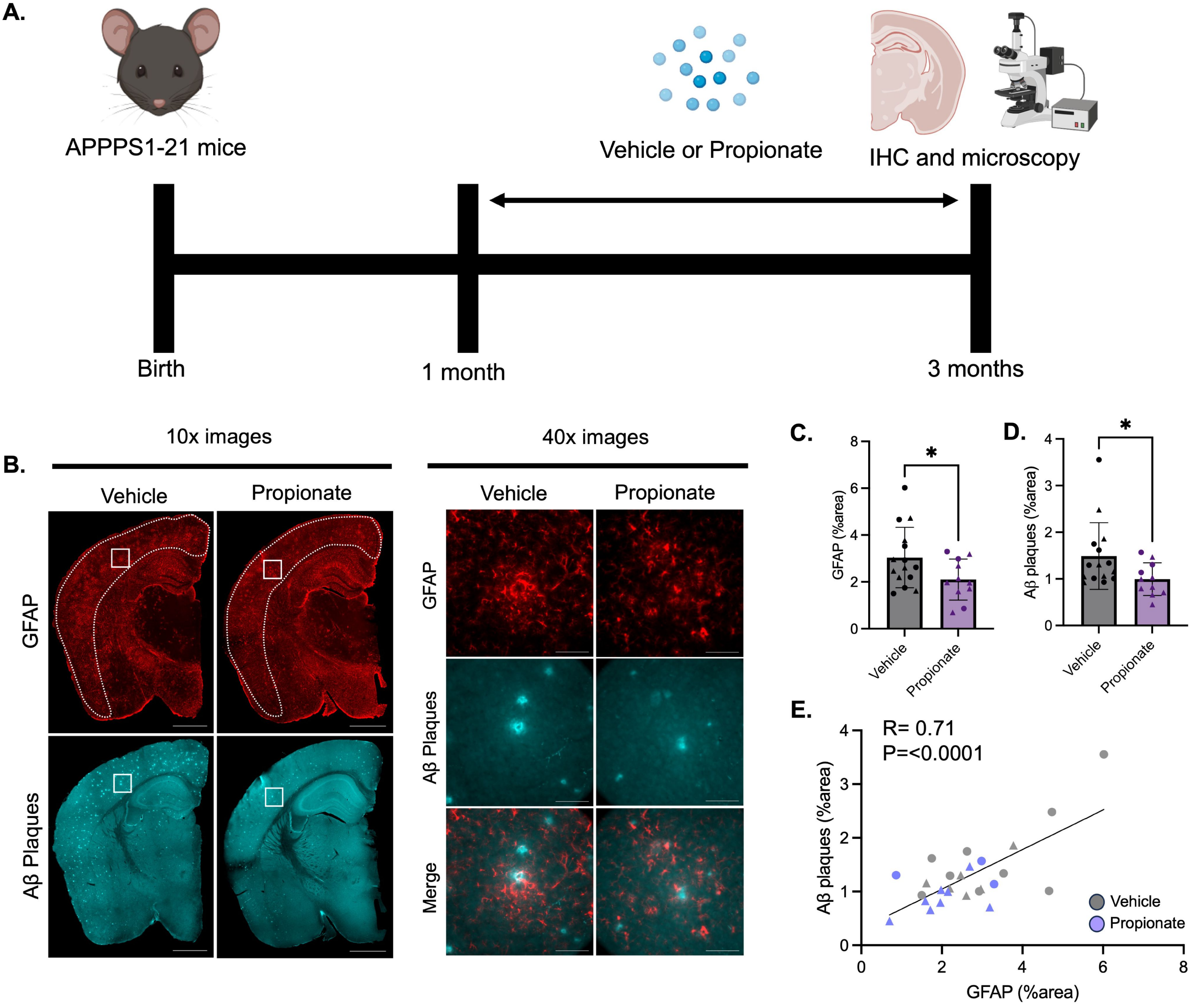

Figure 3: Exogenous propionate treatment reduces GFAP+ astrocytes and Aβ plaques in male and female APPPS1-21 mice.

(A) Schematic depicting experimental paradigm. (B) Representative images of whole brain sections (10x) and cortex (40x) tissue stained for GFAP+ positive astrocytes and Aβ plaques in APPPS1-21 mice treated with vehicle (VHL) control or propionate (PROP). Quantification of cortical (C) GFAP+ astrocyte percent area and (D) Aβ plaque percent area in VHL and PROP treated male and female APPPS1-21 mice. (E) Pearson's correlation analysis between GFAP+ astrocyte percent area and Aβ plaque percent area in VHL and PROP treated male and female APPPS1-21 mice. Data expressed as mean ± standard deviation. N = 11-15/group. Statistics calculated using two-tailed unpaired student's t-tests. 4 sections used per animal. * denotes a p-value ≤ 0.05. Scale bar indicates 1000 μm in 10x images and 100 μm in 40x images. Males denoted by triangles and females denoted by circles. Dotted lines indicate analyzed area of cortex.

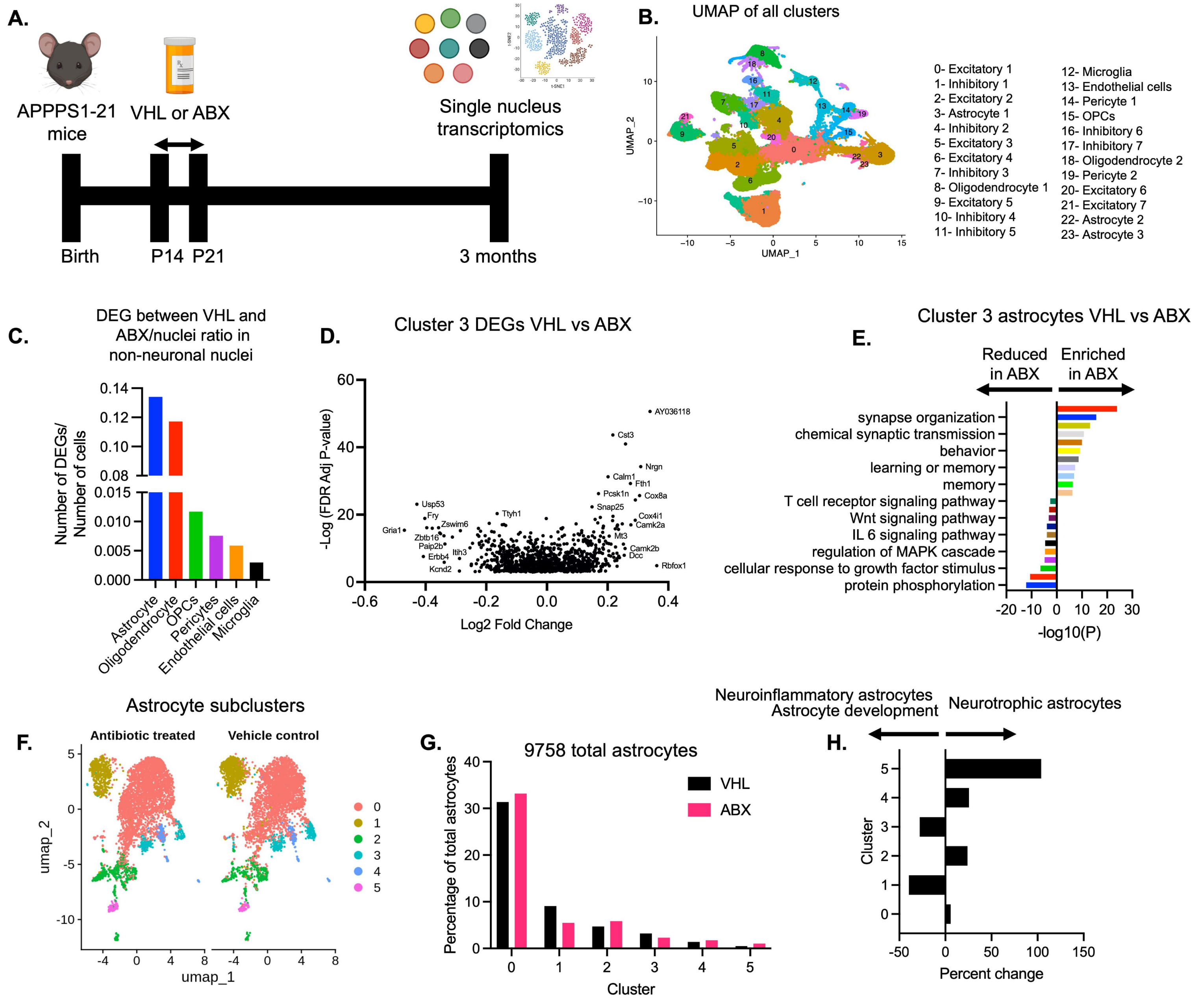

Figure 4: Single nucleus RNA sequencing reveals changes in astrocytic transcription and subclusters upon antibiotic-mediated GMB perturbation in APPPS1-21 male mice.

(A) Schematic depicting experimental paradigm. (B) UMAP plot containing sequenced nuclei from vehicle (VHL) and antibiotic (ABX) treated APPPS1-21 male mice. (C) Number of DEGs per nuclei between VHL and ABX treated mouse non-neuronal nuclei. (D) Volcano plot of DEGs in Cluster 3 astrocytes between VHL and ABX treated mice. (E) Pathway analysis depicting up and down-regulated molecular pathways in Cluster 3 astrocytes between VHL and ABX treated mice. (F) UMAP analysis of Clusters 3, 22, and 23 from UMAP in B identified 6 subclusters (0-5) of astrocytes in the VHL and ABX treated APPPS1-21 mice. (G) Percentage of astrocyte subclusters in VHL and ABX treated mice. (H) Percent change in astrocyte subclusters between VHL and ABX treated mice. DEGs and pathways determined using MAST and Metascape, respectively, with a Log2FC cutoff of 0.25 and an FDR cutoff of 0.001.

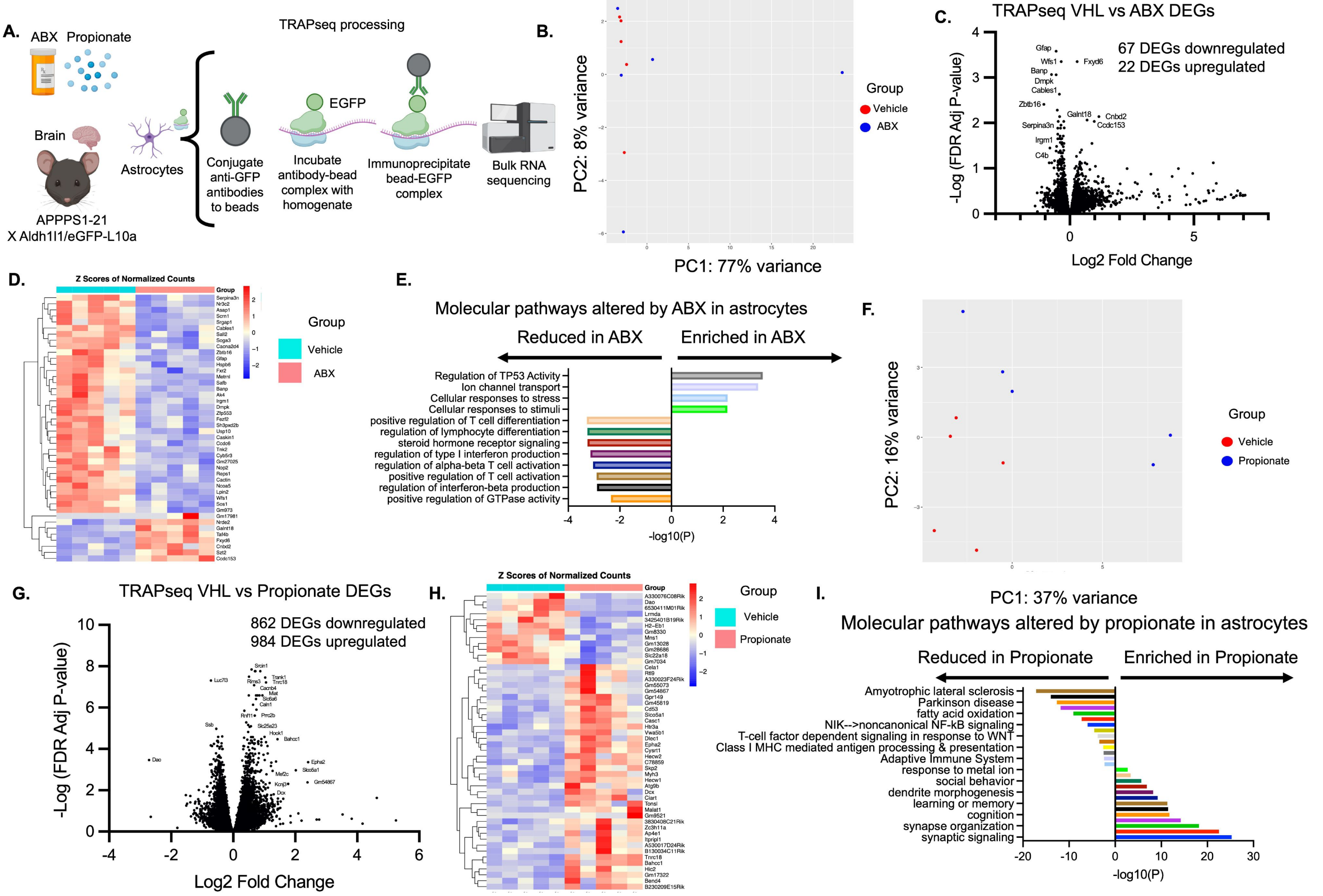

Figure 5: TRAP sequencing reveals changes in astrocytic transcription upon antibiotic-mediated GMB perturbation and exogenous propionate treatment in APPPS1-21 mice.
(A) Schematic depicting experimental paradigm. (B) PCA plot of vehicle (VHL) and antibiotic (ABX) treated TRAPseq samples. (C) Volcano plot of DEGs in ABX treated compared to VHL treated APPPS1-21 male mice. (D) Heatmap depicting top upregulated and downregulated DEGs in ABX treated compared to VHL treated APPPS1-21 male mice. (E) Pathway analysis depicting up and down-regulated molecular pathways in astrocytes between VHL and ABX treated mice. (F) PCA plot of VHL and Propionate (PROP) treated TRAPseq samples. (G) Volcano plot of DEGs in PROP treated compared to VHL treated APPPS1-21 male mice. (H) Heatmap depicting top upregulated and downregulated DEGs in PROP treated compared to VHL treated APPPS1-21 male mice. (I) Pathway analysis depicting up and down-regulated molecular pathways in astrocytes between VHL and PROP treated mice. N= 5/group. DEGs determined using DESeq2 with an FDR cutoff of 0.1. Pathway analysis conducted using Metascape.

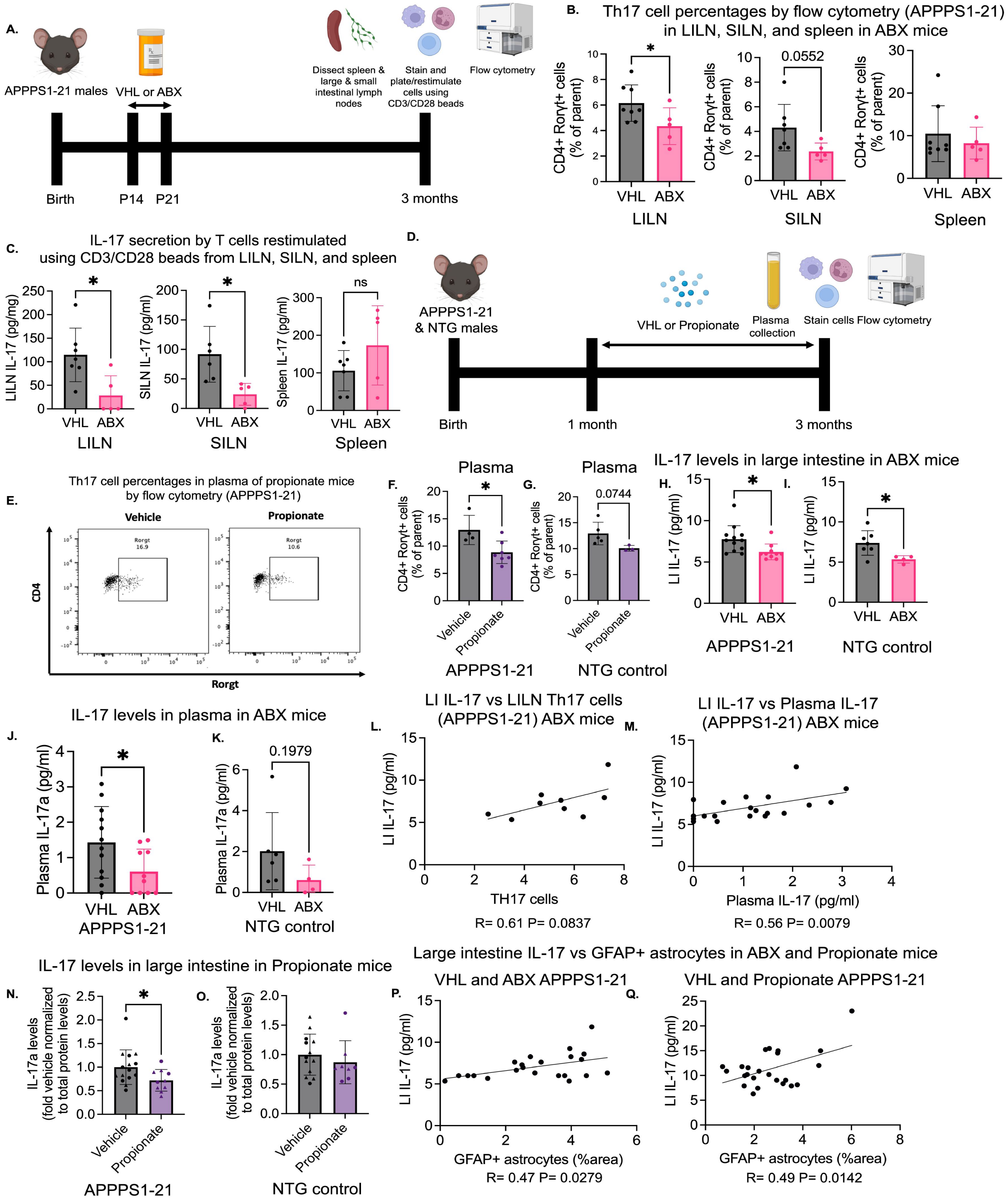

Figure 6: Antibiotic and propionate treatments reduce peripheral Th17 cells and IL-17 levels which correlate positively with GFAP+ reactive astrocytosis in APPPS1-21 mice.

(A) Schematic depicting experimental paradigm for antibiotic (ABX) treated APPPS1-21 male mice. (B) Th17 cell percentages by flow cytometry in LILN, SILN, and spleen in vehicle (VHL) and ABX treated APPPS1-21 mice. (C) IL-17 levels in the media of CD3/CD28 bead-restimulated T-cells derived from the LILN, SILN, and spleen in VHL and ABX treated APPPS1-21 mice. (D) Schematic depicting experimental paradigm for propionate (PROP) treated APPPS1-21 and non-transgenic male mice. (E) Representative flow cytometry plot depicting a reduction in Th17 cells in the plasma of PROP treated APPPS1-21 mice. Quantification of Th17 cell percentages by flow cytometry in the plasma of VHL and PROP treated (F) APPPS1-21 and (G) NTG mice. Quantification of IL-17 levels via ELISA in the large intestine of VHL and ABX treated (H) APPPS1-21 and (I) NTG mice. Quantification of IL-17 levels via ELISA in the plasma of VHL and ABX treated (J) APPPS1-21 and (K) NTG mice. (L) Pearson's correlation analysis between LILN Th17 cells and large intestinal IL-17 levels in VHL and ABX treated APPPS1-21 mice. (M) Pearson's correlation analysis between plasma IL-17 and large intestinal IL-17 levels in VHL and ABX treated APPPS1-21 mice. Quantification of IL-17 levels via ELISA and normalized to total protein in the large intestine of VHL and PROP treated (N) APPPS1-21 and (O) NTG mice. Pearson's correlation analysis between GFAP+ astrocyte percent area and large intestinal IL-17 levels in (P) VHL and ABX and (Q) VHL and PROP treated APPPS1-21 mice. Data expressed as mean ± standard deviation. N = 5-14/group. Statistics calculated using two-tailed unpaired student's t-tests. * denotes a p-value ≤ 0.05, ** indicates p-value ≤ 0.01, *** indicates p-value ≤ 0.001, and **** indicates a p-value of ≤ 0.0001. Males denoted by triangles and females denoted by circles.

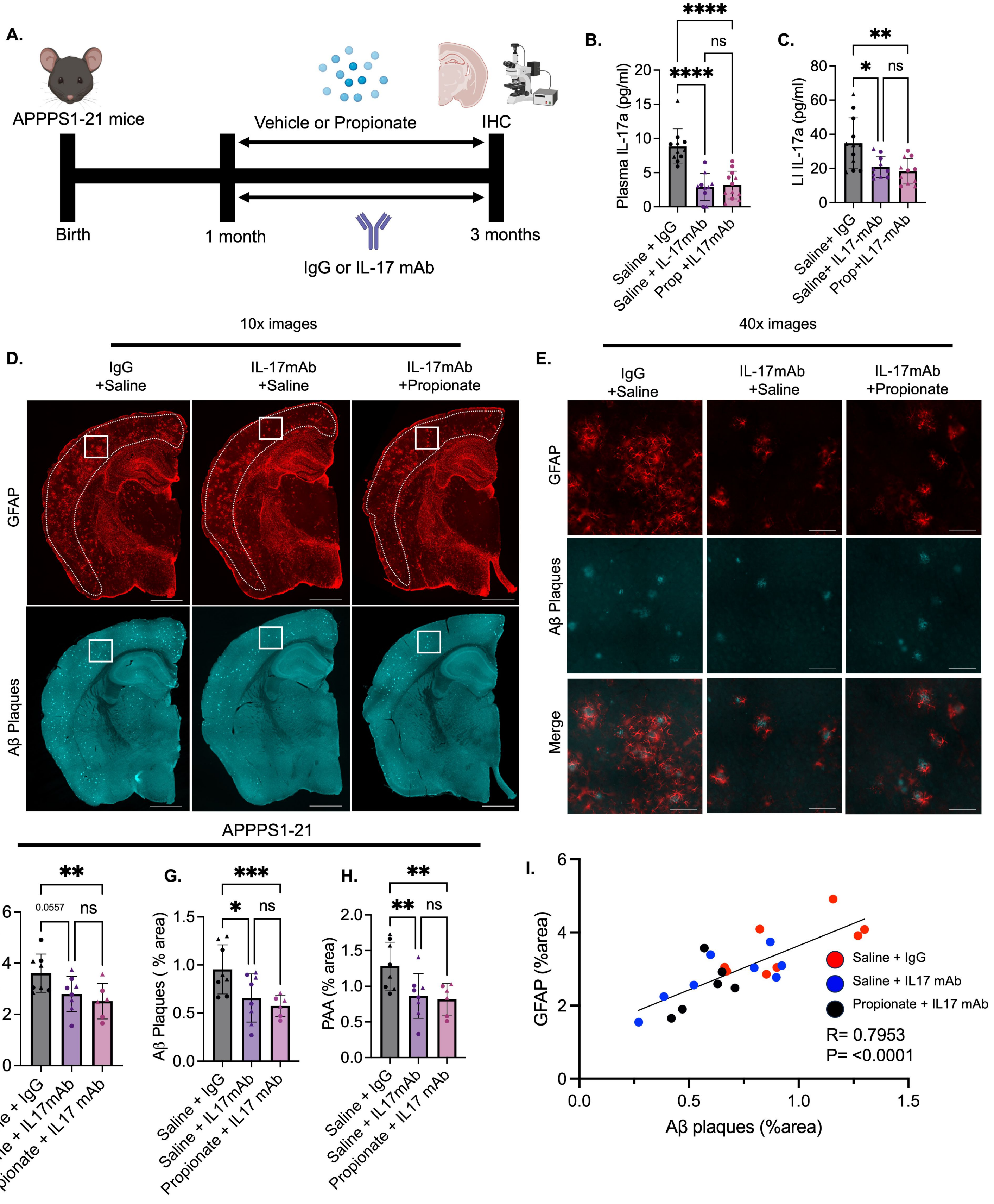

Figure 7: Propionate-induced reductions in GFAP+ reactive astrocytosis and Aβ amyloidosis are dependent on IL-17 signaling in APPPS1-21 mice.

(A) Schematic depicting experimental paradigm. (B) Plasma IL-17 levels in APPPS1-21 male and female mice treated with saline + IgG, saline + IL-17 monoclonal antibody (mAb), or propionate + IL-17 mAb. (C) Large intestinal levels of IL-17 in saline + IgG, saline + IL-17 mAb, and propionate + IL-17 mAb groups. Representative images of GFAP+ astrocytes and Aβ plaques in saline + IgG, saline + IL-17 mAb, and propionate + IL-17 mAB groups taken at (D) 10x and (E) 40x magnifications. Quantification of percent areas of (F) GFAP+ astrocytes, (G) Aβ plaques, and (H) plaque-associated astrocytes (PAA) in saline + IgG, saline + IL-17 mAb, and propionate + IL-17 mAb groups. (I) Pearson's correlation analysis between percent areas of GFAP+ astrocytes and Aβ plaques. Data expressed as mean ± standard deviation. N = 6-12/group. Statistics calculated using two-way ANOVA. 4 sections used per animal. * denotes a p-value ≤ 0.05, ** indicates p-value ≤ 0.01, *** indicates p-value ≤ 0.001, and **** indicates a p-value of ≤ 0.0001. Scale bar for 10x magnification indicates 1000 µm and for 40x indicates 100 µm. Males denoted by triangles and females denoted by circles. Dotted lines indicate analyzed area of cortex.

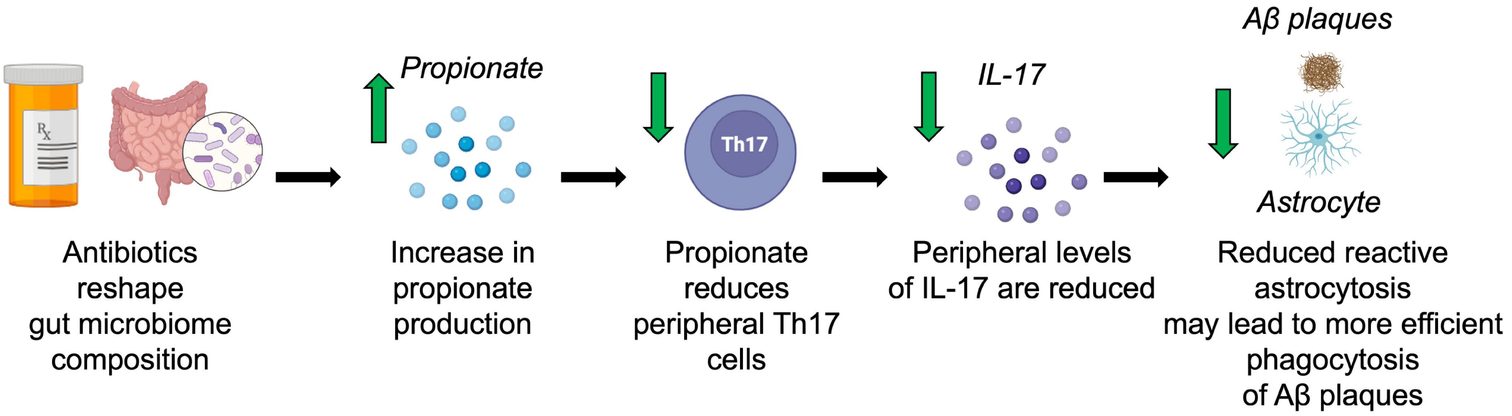

Figure 8: Hypothesis of abx-mediated gut microbiome control of reactive astrocytosis and Aβ amyloidosis Antibiotics reshape gut microbial composition (i.e., increased *Akkermansia*) which leads to changes in levels of gut-derived metabolites, such as the identified increase in propionate. Propionate reduces peripheral Th17 cells and IL-17 production in the periphery which likely leads to lower concentrations in the CNS. IL-17 activates astrocytes and may compromise their ability to phagocytose Aβ plaques. The identified propionate-induced decreases in reactive astrocytosis and Aβ plaques are dependent on IL-17 signaling.